frontiers | Frontiers in Earth Science

TYPE Original Research
PUBLISHED 06 February 2023
DOI 10.3389/feart.2023.1013014

OPEN ACCESS

EDITED BY
Costanza Bonadiman,
University of Ferrara, Italy

REVIEWED BY
Xiaojing Lai,
China University of Geosciences Wuhan, China
Cristina Perinelli,
Department of Earth Sciences, Faculty of Mathematics, Physics, and Natural Sciences, Sapienza University of Rome, Italy
Vincenzo Stagno,
Sapienza University of Rome, Italy

*CORRESPONDENCE
Luca Toffolo,
luca.toffolo@unimi.it

†PRESENT ADDRESS
Francesca Miozzi,
Earth and Planets Laboratory, Carnegie Institution for Science, Washington, DC, United States

SPECIALTY SECTION
This article was submitted to Petrology, a section of the journal Frontiers in Earth Science

RECEIVED 06 August 2022
ACCEPTED 02 January 2023
PUBLISHED 06 February 2023

CITATION
Toffolo L, Tumiati S, Villa A, Fumagalli P, Amalfa A and Miozzi F (2023), Experimental dissolution of carbonaceous materials in water at 1 GPa and 550°C: Assessing the role of carbon forms and redox state on COH fluid production and composition during forearc subduction of organic matter.
Front. Earth Sci. 11:1013014.
doi: 10.3389/feart.2023.1013014

Experimental dissolution of carbonaceous materials in water at 1 GPa and 550°C: Assessing the role of carbon forms and redox state on COH fluid production and composition during forearc subduction of organic matter

Luca Toffolo [1]*, Simone Tumiati [1], Alberto Villa [2], Patrizia Fumagalli [1], Andrea Amalfa[1] and Francesca Miozzi[1†]

[1]Dipartimento di Scienze della Terra "Ardito Desio", University of Milan, Milan, Italy, [2]Dipartimento di Chimica, University of Milan, Milan, Italy

Biogenic carbonaceous material (CM) is the main carrier of organic carbon in the subduction zone and contributes to COH fluid production and volcanic arc gaseous emissions. Here we investigated the effect of the structural, textural and chemical heterogeneity of CM on its reactivity and redox dissolution by conducting short-lived (1 h) experiments, where synthetic analogues of CM (ordered graphite, graphite oxide (GO), mesoporous carbon (MC), Vulcan® carbon (VC) and glass-like carbon (GC)), are reacted with water at P = 1 GPa and T = 550°C—conditions typical of a warm forearc subduction—and fO_2 buffered from ΔFMQ ≈ +4 to −7. We show that the amount of dissolved CM ($CM_{dissolved}$) and the proportion of volatile carbon species ($C_{volatile}$) in the fluid is related both to the structure and the peculiar surficial properties of the carbon forms, such as carbon sp^2-and sp^3-hybridization, amount of oxygen heteroatoms, presence of oxygenated functional groups (OFGs) and of active sites. MC and graphite (C(sp^2) > 93 at%, O < 1 at%, OFGs < 2.3 at%, high proportion of active sites) are relatively inert ($CM_{dissolved}$ < .4 mol%) but the former reacts more extensively at extreme redox conditions (producing CO_2 + CO and CO_2 + CH_4 $C_{volatile}$ mixtures at ΔFMQ ≈ +4 and −7, respectively), while the latter has a maximum of $C_{volatile}$ production (CO_2 + CH_4) at ΔFMQ ≈0, which is not observed in a 10-day long run; partly-ordered GO (C(sp^3) > 98 at%, O ~31 at%, OFGs ~41 at%) is the most reactive material at all redox conditions ($CM_{dissolved}$ > 2.6 mol%) and produces CO_2 as the dominant $C_{volatile}$ species; disordered GC and VC (C(sp^3) < 30 at%, O < 8 at%, OFGs < 30 at%) are more reactive at ΔFMQ ≈ +4 ($CM_{dissolved}$ ~1 mol %) and ΔFMQ ≈ −7 ($CM_{dissolved}$ > 1 mol%), where $C_{volatile}$ is dominantly CO_2 and CH_4, respectively. Besides the significant deviations from thermodynamically predicted graphite-saturated COH fluid composition and speciation, our results suggests that: 1) immature CM (disordered, rich in C(sp^3), O, OFGs) is preferentially dissolved under high fluid fluxes and may buffer fluids to rather oxidizing conditions; 2) a descending flux of oxygen (and hydrogen) bond to CM may exist.

KEYWORDS

carbonaceous matter, graphite, subduction, experimental petrology, COH fluids, dissolution

1 Introduction

Graphitic carbon and other carbonaceous materials (CM) derived from biogenic organic matter are ubiquitous components of (meta) sedimentary rocks and they are the main carrier of reduced carbon to the mantle through subduction zones (Hayes and Waldbauer, 2006; Plank and Manning, 2019). This flux of subducted organic carbon sequestered from the biosphere (estimated to ~12 Mt yr^{-1}; Plank and Manning, 2019) is involved in the production of carbon-bearing fluids, which can metasomatize the mantle wedge and, eventually, escape back to the atmosphere through volcanic arc gaseous emissions, possibly influencing long-term oscillations of Earth's climate (Hayes and Waldbauer, 2006; Mason et al., 2017; Tumiati et al., 2017; Plank and Manning, 2019; Tumiati and Malaspina, 2019; Sheik et al., 2020; Vitale Brovarone et al., 2020; Tumiati et al., 2022). Therefore, assessing how and to which extent organic carbon is recycled into the mantle, requires to first understand the processes that can extract it from subducted CM. The key role is played by aqueous fluids originated from the dehydrating subducting slab, which can dissolve carbon either by oxidizing or reducing it into volatile (CO_2, CH_4, and CO) and ionic (both organic and inorganic) species (Connolly and Cesare, 1993; Connolly, 1995; Sverjensky et al., 2014). It has been shown that solubility of CM is influenced by its crystallinity, with disordered glass-like forms being less refractory than graphite at depths < ~110 km, hence potentially leading the organic carbon flux at forearc to sub-arc metamorphic conditions (Tumiati et al., 2020; Vitale Brovarone et al., 2020). Biogenic CM, in fact, gains a perfectly ordered graphitic structure either at high grades of metamorphism (T > ~650°C; Beyssac et al., 2002a) or when precipitated from COH fluids (Luque et al., 1998). In the other cases, it exhibits heterogeneous structures and microtextures, which can coexist in the same sample at the nanometer to the micrometer scale and can be substantially different in rocks that experienced similar metamorphic conditions (Buseck and Huang, 1985; Beyssac et al., 2002b; 2003). These effects can be ascribable to the presence of diverse organic precursors (e.g., graphitizing or non-graphitizing) and to the previous tectono-metamorphic history of the rock, including the early presence of fluids that can dissolve or precipitate carbon (Buseck and Huang, 1985; Beyssac and Rumble, 2014; Vitale Brovarone et al., 2020). Moreover, CM can also contain H and other elements, such as O, N, P, S (heteroatoms), typically bond to its carbon skeleton, which are progressively lost with the increasing grade (e.g., Buseck and Huang, 1985; Vandenbroucke and Largeau, 2007; Buseck and Beyssac, 2014). This variety of structural, microtextural and chemical features in turn affect the reactivity of CM and hence its dissolution kinetics (Beyssac et al., 2002a; Buseck and Beyssac, 2014; Tumiati et al., 2020; Vitale Brovarone et al., 2020). Raman spectroscopy coupled to TEM imaging and diffraction have been customarily used to evaluate the level of crystallinity of CM and its microtexture (Beyssac et al., 2002b; Buseck and Beyssac, 2014). However, they cannot directly detect some of the fundamental features that affect the tendency of CM to react and graphitize, i.e., carbon hybridization—essentially sp^2 vs. sp^3 bond configuration—and presence of heteroatoms, the former indicating the aromatic or aliphatic character of CM, the latter being mainly related to oxygenated functional groups (Buseck and Huang, 1985; Vandenbroucke and Largeau, 2007; Hazen et al., 2013; Buseck and Beyssac, 2014). Rather, this information can be provided by other spectroscopic techniques commonly employed in material sciences, such as X-ray photoelectron spectroscopy (XPS; e.g., Barlocco et al., 2020).

In this paper we use synthetic carbon forms—characterized by various degrees of crystallinity, proportions of sp^2-and sp^3-hybridized carbon, as well as oxygenated functional groups—to experimentally investigate the solubility in water of CM at P = 1 GPa, T = 550°C and redox conditions ranging from ΔFMQ ≈ +4 to −7. We show how both the structure and the surface properties of CM together with the system redox state influence the amount of dissolved carbon and the composition of produced COH fluids. By relating the considered synthetic carbon forms to natural CM, we could extrapolate our results to subduction environments, providing insights on the reactivity of CM in the low-temperature forearc regions of subduction zones and in particular in the slab surface, where metasediments containing reduced carbon can conceivably interact with aqueous fluids originated from the dehydrating lithosphere.

2 Materials and methods

2.1 Experimental strategy

We used as starting materials five commercially available synthetic carbon forms, i.e., glass-like carbon (GC), synthetic graphite, graphite oxide (GO), mesoporous carbon (MC) and Vulcan® carbon (VC; see Appendix A for a summary of each CM feature). Each material was supplied as a fine-grained powder. The choice of synthetic rather than natural CM was dictated by the necessity of using homogenous materials with a standard composition with the purpose of facilitating potential links between their physicochemical properties and their solubility. We prepared the runs by filling an $Au_{60}Pd_{40}$ alloy capsule (outer diameter: 2.3 mm; wall thickness: .15 mm) with the carbon powder and ~1 μL of pure water (MilliQ), previously boiled in a N_2 stream to remove dissolved atmospheric CO_2. Redox state in the capsule was buffered by using the double capsule technique (Eugster, 1957; Eugster and Skippen, 1967; Figure 1): the capsule containing the sample is inserted along with a solid buffer assemblage and water in a larger gold capsule (outer diameter: 4.5 mm); at the run P–T conditions water equilibrates with the solid buffer and dissociates producing H_2 (e.g., Eugster, 1957; Frost, 1991), which will diffuse through the wall of the $Au_{60}Pd_{40}$ inner capsule until the same fH_2 is established in the two capsules; at given P and T, the external control of fH_2 also fixes fO_2 in the inner capsule through the reaction (Eq. 1)

$$H_2 + \frac{1}{2}O_2 = H_2O \quad (1)$$

from which:

$$K = \frac{f_{H_2O}}{f_{H_2} \cdot (f_{O_2})^{\frac{1}{2}}}$$

where K is the equilibrium constant (Shaw, 1963).

We used a series of five buffering assemblages, listed below, along with their controlling reactions, from the more oxidizing to the more reducing (Supplementary Figure S1):

- MH, magnetite–hematite: $2Fe_3O_4 + H_2O \rightleftharpoons 3Fe_2O_3 + H_2$;
- NNO, nickel–nickel oxide: $Ni + H_2O \rightleftharpoons NiO + H_2$;
- FMQ, fayalite–magnetite–quartz: $3Fe_2SiO_4 + 2H_2O \rightleftharpoons 2Fe_3O_4 + 3SiO_2 + 2H_2$;
- WM, wüstite–magnetite: $3FeO + H_2O \rightleftharpoons Fe_3O_4 + H_2$;
- H_2O-H_2, water–hydrogen: $2H_2O \rightleftharpoons 2H_2 + O_2$

10.3389/feart.2023.1013014

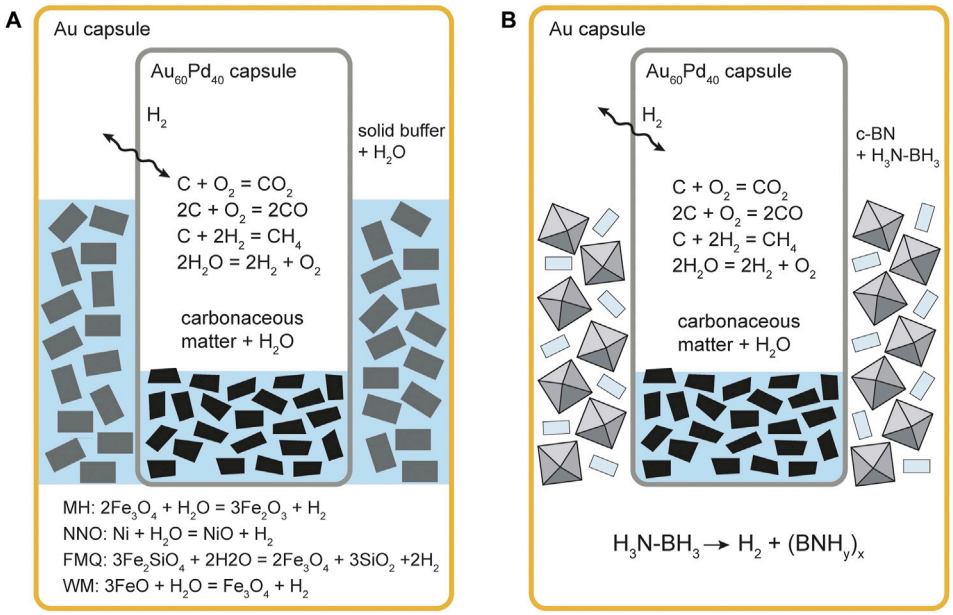

FIGURE 1
Schematic representation of the double capsule setups used to buffer fH_2 in our experiments. **(A)** solid buffer assemblages; **(B)** water-hydrogen buffer. The relevant fH_2-buffering reactions are shown together with the equilibria that involve the COH fluid in the inner capsule. In **(B)** ammonia borane is mixed with grains of inert cubic boron nitride (c-BN) to prevent the collapse of the outer capsule.

TABLE 1 fO_2 and fH_2 in the external (out) and internal (in) capsule and compositions of COH fluid in equilibrium with either graphite or glass-like carbon calculated for the indicated buffers at 550°C, 1 GPa. See Section 2.2.2 for the details of the calculation.

	MH	NNO	FMQ	WM	H_2O-H_2
$\log(fO_2/1\ bar)_{out}$	-16.9	-20.4	-20.5	-26.0	-27.6
ΔFMQ	+4	+0.2	0	-5	-7
$fH_{2\ out\ =\ in}$	0.415	24.1	28.7	16000	101000
$\log(fH_2/1\ bar)_{in}$	-0.38	1.4	1.5	4.2	5.0
$\log(fO_2/1\ bar)_{in}$	-19.7	-20.5	-20.6	tending to −∞	tending to −∞
COH fluid in equilibrium with graphite (mole fractions)					
H_2O	0.02	0.90	0.93	0	0
CO_2	0.98	0.10	0.07	0	0
CO	0	0	0	0	0
CH_4	0	0	0	1	1
H_2	0	0	0	0	0
COH fluid in equilibrium with glass-like carbon (mole fractions)					
H_2O	0	0.88	0.91	0	0
CO_2	1	0.12	0.09	0	0
CO	0	0	0	0	0
CH_4	0	0	0	1	1
H_2	0	0	0	0	0

10.3389/feart.2023.1013014

TABLE 2 Run table of the experiments. The starting materials are abbreviated as follows: GO, graphite oxide; MC, mesoporous carbon; VC, Vulcan® carbon; GC, glass-like carbon.

Run ID	Starting materials	Buffer	CM amount (mg)	Run duration (h)	*P* (GPa)	*T* (°C)
COH180	graphite + H_2O	MH	4.39	1	1	550
COH145	graphite + H_2O	NNO	3.12	1	1	550
COH189	graphite + H_2O	FMQ	1.82	1	1	550
COH149	graphite + H_2O	WM	4.17	1	1	550
COH181	graphite + H_2O	H_2O-H_2	8.05	1	1	550
COH166	graphite + H_2O	FMQ	6.53	240	1	550
COH163	GO + H_2O	MH	2.89	1	1	550
COH164	GO + H_2O	NNO	3.59	1	1	550
COH162	GO + H_2O	FMQ	4.31	1	1	550
COH165	GO + H_2O	WM	5.13	1	1	550
COH177	GO + H_2O	H_2O-H_2	9.14	1	1	550
COH175	MC + H_2O	MH	2.47	1	1	550
COH156	MC + H_2O	NNO	5.12	1	1	550
COH154	MC + H_2O	FMQ	4.25	1	1	550
COH157	MC + H_2O	WM	6.63	1	1	550
COH182	MC + H_2O	H_2O-H_2	4.42	1	1	550
COH151	VC + H_2O	MH	3.80	1	1	550
COH152	VC + H_2O	NNO	3.93	1	1	550
COH150	VC + H_2O	FMQ	2.44	1	1	550
COH153	VC + H_2O	WM	2.64	1	1	550
COH174	VC + H_2O	H_2O-H_2	3.87	1	1	550
COH159	GC + H_2O	MH	8.97	1	1	550
COH160	GC + H_2O	NNO	9.15	1	1	550
COH158	GC + H_2O	FMQ	15.30	1	1	550
COH161	GC + H_2O	WM	7.77	1	1	550
COH176	GC + H_2O	H_2O-H_2	6.79	1	1	550
COH203	dried green microalgae (*Tetraselmis suecica*)	-	150	72	1	550

While the MH, NNO, FMQ and WM are well-known buffering assemblages commonly employed in experimental petrology (e.g., Eugster, 1957; Shaw, 1963; Myers and Eugster, 1983; Frost, 1991; Tumiati et al., 2017; Tumiati et al., 2020), we obtained H_2O–H_2 buffered conditions by a novel approach that involves the thermolysis of ammonia borane (H_3N-BH_3) in the outer capsule. At 1 GPa and 550°C, ammonia borane decomposes almost completely into hydrogen gas and a solid precursor to hexagonal BN (i.e., polymeric $(BNH_y)_x$, where y << .5; Nylén et al., 2009). With this expedient fH_2 becomes very high in the inner capsule as well, where a mixed H_2O-H_2 fluid forms, constraining fO_2 to very reducing conditions. Solid cubic boron nitride was mixed with ammonia borane to prevent the collapse of the external capsule during the experiment, since the pyrolysis of ammonia borane is accompanied by a volume decrease, and because it is inert to the decomposition products of ammonia borane at such reducing conditions. The oxygen and hydrogen fugacities (fO_2 and fH_2) of the various buffers at the experimental conditions are reported in Table 1.

To reach the conditions of 1 GPa and 550°C we used a rocking end loaded piston cylinder apparatus (University of Milan). The double capsule was positioned in the middle of an assembly (full salt-type) consisting of an inner MgO rod (BN rod for H_2O–H_2 buffered runs) through which a K-type thermocouple (with a precision of ±5°C) is inserted, a graphite furnace, and an outer cylinder made of NaCl (pressure medium). A .6 mm-thick Al_2O_3 disk (or AlN disk for runs buffered by H_2O–H_2) is interposed between the thermocouple and the capsule to avoid accidental perforation of the external capsule during the run. Electric current flows through the graphite furnace from a pyrophyllite-steel plug to a graphite disk placed at the base of the assembly. We used the quartz to coesite transition as pressure

calibration of the experimental apparatus (Bose and Ganguly, 1995), which gives an accuracy of the sample pressure of ±.01 GPa. We carried out a set of 25 experiments by combining the five carbon forms and the five buffers (Table 2). In each experimental run the samples were first compressed to 1 GPa then heated to 550°C following a 100°C/min ramp. The high *P–T* conditions were maintained for 1 h: short run durations are mandatory to investigate, even if far from thermodynamic equilibrium, the redox dissolution properties of metastable CM very prone to structural/chemical re-organization. An additional 240-h long experiment (COH166) was carried out at the same *P–T* conditions and FMQ-buffered fO_2 using ordered graphite, a thermodynamically stable phase at the *P–T* investigated, to test its long-term reactivity at conditions approaching thermodynamic equilibrium. All the experiments were terminated by quenching with a >40°C/s temperature drop, in order to preserve both the bulk {C, O, H} composition and the speciation of the fluids (Tiraboschi et al., 2016; Tumiati et al., 2017; Tumiati et al., 2020; Tiraboschi et al., 2022). At the end of every experiment, the external capsule was first cleaned with a concentrated HCl solution, then partially peeled to expose the inner capsule and placed in a vacuum oven at 110°C for ~2 h to completely remove the water that impregnated the buffer. The dried capsules were mounted in epoxy resin and then pierced to analyze the volatile phases (Section 3.2 for the details); afterwards, the inner capsules were opened and the solids extracted. The preservation of the buffering assemblages and the almost total decomposition of ammonia borane after every experimental run was ascertained by means of energy-dispersive X-ray spectroscopy and both backscattered and secondary electron imaging performed with a JEOL 8200 electron microprobe (University of Milan).

2.2 COH fluid composition

2.2.1 QMS analysis

We extracted the volatile phases trapped in the inner capsule, which are expected to consist of a dominantly aqueous liquid and a non-condensable carbon-rich gas phase, by using the capsule-piercing apparatus devised by Tiraboschi et al. (2016) and then we analyzed them by means of quadrupole mass spectrometry (QMS) using an EXTORR 0–200 amu, Mod. XT 200, mass spectrometer equipped with a secondary electron multiplier (University of Milan). Every capsule was placed in a reactor heated to 90°C and pierced; after that, the volatiles were conveyed by a pure Ar flux to the QMS through an heated line (90°C) to prevent water condensation. In each *m/z* channel of the QMS the signal was collected for 1,545 s and then it was integrated by using an expressly created Wolfram Mathematica® routine. The QMS was calibrated by utilizing as standards pure H_2O and H_2, and known mixtures of CO_2-O_2 and CO-CH_4. Uncertainties in the measurements were estimated to be ~1 mol% for H_2O, CO_2, CH_4, H_2 and O_2 but 10 mol% for CO due to the interference with air (nitrogen) on the 28 *m/z* channel. The reproducibility of the measurements was periodically verified by analyzing the amounts of H_2O, CO, CO_2 and H_2 produced by the thermal decomposition at 250°C of 1 mg of oxalic acid dihydrate contained in test capsules (Tiraboschi et al., 2016).

2.2.2 Thermodynamic modeling of COH fluids

We used thermodynamic modeling to estimate the redox state (expressed as oxygen fugacity, fO_2, and hydrogen fugacity, fH_2) in both the outer and the inner capsule and to obtain a model of the speciation of a COH fluid in equilibrium with either graphite or glass-like carbon to be compared to our experimental results (Table 1). We carried out these calculations by using the Perple_X software package (Connolly, 2005), supported by a version of the thermodynamic database of Holland and Powell (Holland and Powell, 1998) that we modified to include the updated thermodynamic data for Ni, NiO and wüstite (hp04ver_mod.dat; Miozzi and Tumiati, 2020). In particular, we used the equation of state (EoS) "H-O MRK hybrid" integrated in the Perple_X routine "fluids" to determine the fH_2 in the external capsule at the fO_2 fixed by the various buffers; then, knowing that fH_2 is the same in both the capsules ($fH_{2,\,ext} = fH_{2,\,int}$), we obtained the fO_2 in the internal capsule with the "C-buffered COH MRK hybrid-EoS" (Connolly and Cesare, 1993). The same EoS was used to calculate the speciation of the fluid in equilibrium either with graphite or glass-like carbon; in the latter case the activity of carbon was assumed to be 1.09 (Tumiati et al., 2020; Vitale Brovarone et al., 2020, for a detailed description of the method).

2.3 Characterization of the solid phases

Micro-Raman spectroscopy and transmission electron microscopy (TEM) were used on both the starting material and recovered experimental products, to verify the occurrence of modifications in the in the structure and crystallinity of the carbonaceous material. In addition to this, the starting materials and the CM samples used for comparison were analyzed by using X-ray photoelectron spectroscopy (XPS) to investigate the hybridization of carbon, the proportion of C and O atoms and the presence of oxygenated functional groups. This technique could not be applied to solid CM retrieved from experimental capsules due to the small available quantities, with the exception of run COH203 (char from pyrolysis of green microalgae) that was carried out in a large single capsule (Section 3.3.4).

2.3.1 Micro-Raman spectroscopy

Micro-Raman spectroscopy was carried out using a Horiba LabRam HR Evolution ultra low frequency (ULF) spectrometer (University of Milan) equipped with a Nd-Yag 532 nm/100 mW laser. Scattered light was collected by a 100× objective (NA aperture = 0.9) in backscattering geometry; a diffraction grating with 600 lines/mm and a hole of 300 μm were used. The Raman spectra were detected by a Peltier-cooled CCD detector. In order to avoid CM disordering induced by the laser source the power was set to ~1 mW, as measured on the sample by a power meter. To balance the signal-to-noise ratio, each acquisition (up to 300 s long) was accumulated twice. Instrument calibration was performed before each set of analysis using the peak at 520.70 cm^{-1} of a silicon wafer. We obtained the Raman spectra directly on starting powders and on solids extracted from experimental capsules or separated from natural samples. No mechanical or chemical preparation was involved in the analysis of starting materials or of experimental products. We relied on the work of Beyssac and Lazzeri (2012) to identify the characteristic Raman peaks of the carbon materials.

2.3.2 TEM

We obtained images of the structure and texture of synthetic and natural CM by using a Tecnai F20 high resolution field emission

microscope (TEM facility of the Unitech COSPECT, University of Milan), operating at a maximum accelerating voltage of 200 kV and equipped with an X-TWIN objective lens and an energy-dispersive X-ray spectrometer. Selected area electron diffraction (SAED) patterns were also acquired. In order to perform the analyses, the samples were dispersed in ethanol and a droplet of the suspension was then poured on a holey amorphous carbon support grid.

2.3.3 XPS

XPS was used to examine the surface properties of the carbon materials. A Thermo Scientific K-alpha+ spectrometer was used (University of Milan). The samples were analyzed using a monochromatic Al X-Ray source operating at 72 W, with the signal averaged over an oval-shape area of 600 × 400 µm. Data were recorded at 150 eV for survey scans and 40 eV for high resolution (HR) scans with a 1 eV and .1 eV step size, respectively. Data were processed with CASAXPS software (v2.3.17 PR1.1), using Scofield sensitivity factors and energy exponent of −.6. XPS survey analysis reveals the proportion of carbon and oxygen atoms. The deconvolution of HR C 1s spectra allows to evaluate the relative concentration of sp^2- (at an average binding energy, B.E., of ~284.2 V) and sp^3-hybridized carbon species, the latter is either bond as C–C (B.E. ~285.2 eV), or as oxygenated functional group (C–O, C=O, O=C–OH; components at B.E ≥ 285.7 eV). The components of the HR C 1s spectra were pinpointed according to Xie et al. (2010).

2.3.4 Preparation of CM used for comparison purposes

In order to compare our synthetic carbon forms to natural analogues, we extracted the CM from two different rock samples (Appendix A): 1) immature kerogen disseminated in a dolomitic rock (DOL) belonging to the Triassic Dolomia Principale Formation from Bazena (Southern Alps, Italy), which experienced a low T (~100°C) burial up to a depth of ~5 km (Berra and Carminati, 2010; Berra et al., 2020); 2) CM forming C-rich layers in a calcschist (TAV-M938) from Tavignano valley (Alpine Corsica, France), metamorphosed at low-grade blueschist conditions slightly colder than those of our experiments (~350°C, .6–1 GPa; Vitale Brovarone et al., 2013). Both rock samples were first crushed and manually ground in an agate mortar. Carbonates were then removed using 10 mL of a 6N HCl solution heated at 80°C for 12 h. The powder was eventually washed with distilled water and centrifuged. The absence of carbonates was checked with X-ray powder diffraction using a Panalytical X'pert Pro diffractometer (University of Milan).

Moreover, to obtain a CM for which the P–T conditions are well constrained, we performed a 72-h long experiment (COH203; Table 2; Appendix A) in which char was produced from the pyrolysis of dried green microalgae (cultured *Tetraselmis suecica*) at 550°C and 1 GPa. To this purpose, a single 5 mm Pt capsule was filled with the material, preliminarily cleaned with distilled water and centrifuged in order to eliminate water-soluble salts. Then the capsule was inserted it into a full salt-type assembly (see Section 3.1) and loaded into a single-stage piston cylinder apparatus (University of Milan).

3 Results

We analyzed the solid carbon extracted from the experimental capsules in order to monitor possible structural modifications occurred along with redox dissolution and or increase in temperature and pressure. All the after-run samples show unchanged Raman peak positions within the analytical uncertainties compared to starting materials (Figure 2; Supplementary Figure S2), with the exception of GO, for which after the experimental run a slight shift of the G and D peaks to lower wavenumbers (i.e., from ~1,605 cm^{-1} to 1,597 cm^{-1} from ~1,354 cm^{-1} to 1,345 cm^{-1}) is noticeable. A small increase in the intensities of the D peaks (related to the amount of defects) is observable for GO and to a minor extent for graphite and MC. TEM imaging and SAED does not reveal any appreciable change in the structure of the different carbon forms.

3.1 Dissolution of CM, COH fluid composition and speciation

All carbon forms do produce a COH fluid at our experimental conditions, however the extent of the dissolution, the speciation and the composition of the fluid phase vary depending on the different carbon forms and redox conditions (Table 3). The proportion of the dissolved volatile carbon species relative to the quantity of carbon inserted into the capsule ($CM_{dissolved}$ = ($C_{volatile\text{-}product}/C_{solid\text{-}starting}$) ·100, where $C_{volatile\text{-}product}$ is the sum of all the volatile carbon species in the product fluid—i.e., CO_2, CH_4 and CO—and $C_{solid\text{-}starting}$ is the mass of carbon inserted in the capsule, all the quantities being expressed in micromoles) is shown in Figure 3. The percentage is highest for GO at all redox conditions ($CM_{dissolved}$ > ~2.6%) and it is maximized at fO_2 comprised between ΔFMQ ≈ +4 and ΔFMQ ≈ 0 ($CM_{dissolved}$ > ~5%). GC and VC dissolve more extensively towards extreme fO_2 conditions, with maxima at ΔFMQ ≈ +4 ($CM_{dissolved}$ ~.70% and $CM_{dissolved}$ ~1.2%, respectively) and ΔFMQ ≈ −7 ($CM_{dissolved}$ ~2.9% and $CM_{dissolved}$ ~1.0%, respectively) and the minima centered at ΔFMQ ≈ 0 for GC and ΔFMQ ≈ +.2 for VC ($CM_{dissolved}$ ~.24% and $CM_{dissolved}$ ~ .16%, respectively). MC, though quite inert, has a similar behavior in that the extent of dissolution increases from the minima at ΔFMQ ≈ 0 and ΔFMQ ≈ −5 ($CM_{dissolved}$ ~0%) towards most oxidizing and reducing conditions, i.e., ΔFMQ ≈ +4 and ΔFMQ ≈ −7 ($CM_{dissolved}$ ~.32% and ~.10%, respectively). Graphite is significantly reactive only at ΔFMQ ≈ 0 ($CM_{dissolved}$ ~.37%).

H_2O is the dominant species in the COH fluids, excluding the experiments buffered at ΔFMQ ≈ −7 carried out on graphite –where H_2 has a molar concentration of ~75%– and on GC or VC –where the main species is CH_4 (~52% or ~46% CH_4, respectively).

The major carbon volatile species is CO_2 ($[CO_2/(CO_2 + CO + CH_4)]_{molar}$ > .5) in most experiments, with some exceptions (Figure 4; Supplementary Figure S3). The mole fraction of CO exceeds that of CO_2 in the experiments containing: 1) MC with fO_2 buffered by MH, FMQ or WM ($[CO/(CO_2 + CO + CH_4)]_{molar,\ MC,\ MH}$ ~.91, $[CO/(CO_2 + CO + CH_4)]_{molar,\ MC,\ FMQ}$ ~.62, $[CO/(CO_2 + CO + CH_4)]_{molar,\ MC,\ WM}$ ~.77, though the last value is affected by a large uncertainty); 2) graphite with fO_2 buffered by NNO and WM ($[CO/(CO_2 + CO + CH_4)]_{molar,\ graphite,\ NNO}$ ~.63, associated, however with a large uncertainty; $([CO/(CO_2 + CO + CH_4)]_{molar,\ graphite,\ WM}$ ~.84); 3) VC with fO_2 buffered by FMQ ($[CO/(CO_2 + CO + CH_4)]_{molar,\ VC,\ FMQ}$ ~.82). Methane shows the highest proportions in the experiments containing graphite buffered by FMQ ($[CH_4/(CO_2 + CO + CH_4)]_{molar,\ graphite,\ FMQ}$ ~.51) and in all the experiments buffered by H_2O-H_2 $[CH_4/(CO_2 + CO + CH_4)]_{molar,\ GC,\ H2O\text{-}H2}$ ~.77, $[CH_4/(CO_2 + CO +$

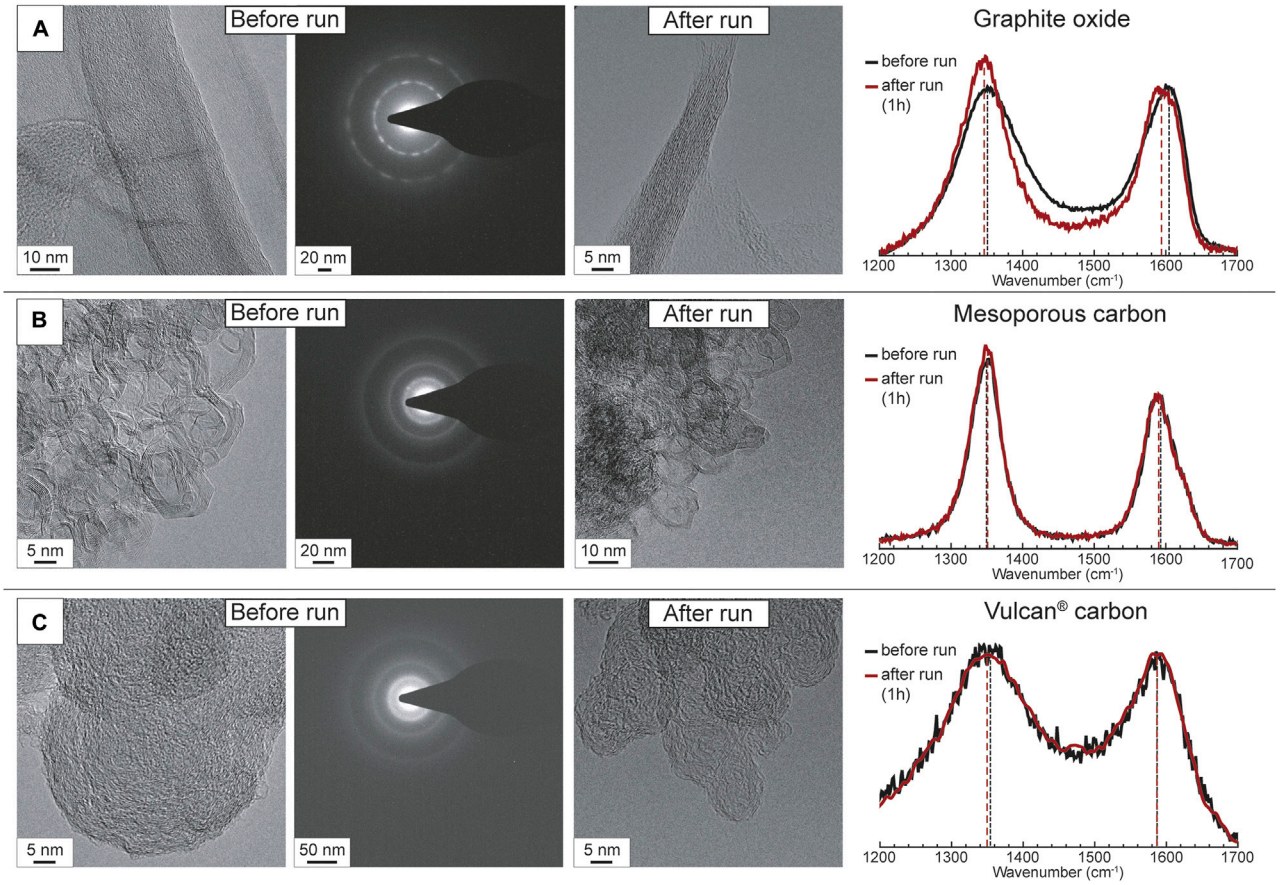

FIGURE 2
Representative TEM images and Raman spectra of **(A)** graphite oxide, **(B)** mesoporous carbon and **(C)** Vulcan® carbon before and after the experimental runs. TEM images of the starting materials are coupled with SAED diffraction patterns to show their degree of structural organization. The intensities of the Raman spectra are normalized to the same scale.

$CH_4)]_{molar,\ graphite,\ H2O\text{-}H2}$ ~.64, $([CH_4/(CO_2 + CO + CH_4)]_{molar,\ MC,\ H2O\text{-}H2}$ ~.56, $([CH_4/(CO_2 + CO + CH_4)]_{molar,\ VC,\ H2O\text{-}H2}$ ~.67), except that in which the carbon form is GO.

4 Discussion

4.1 Reactivity of carbon forms

Since all the experimental runs lasted 1 h (with the exception of the reference graphite-saturated run COH166 approaching thermodynamic equilibrium) and were performed at the same *P–T* conditions, we infer that the diverse solubility of the examined carbon forms arises from their specific reactivity. We exclude any effect due to fluctuations in fH_2 between the inner and outer capsule since equilibration occurs in few minutes at our experimental conditions (Holleck, 1970; Sonwane et al., 2006).

Graphite and MC are the least reactive carbon forms ($CM_{dissolved}$ < .4%). In the experiments containing graphite the amount of dissolved carbon species in the fluid is maximized at ΔFMQ ≈ 0 (and probably at ΔFMQ ≈ +.2, but $CM_{dissolved}$ is affected by a large uncertainty) but it is lowest at ΔFMQ ≈ +4 and ΔFMQ ≈ −7. Even though the dominant volatile carbon species at those extremely oxidizing or reducing fO_2s are either CO_2 or CH_4, respectively, approaching what predicted by thermodynamic modeling (fluid composed of either pure CO_2 at ΔFMQ ≈ +4 or pure CH_4 at ΔFMQ ≈ −7; Table 1; cf. Connolly, 1995), the reactions that produce the two species seem to be inhibited. A clue may be found in the relatively high concentration of H_2 in the fluid at both ΔFMQ ≈ +4 and ΔFMQ ≈ −7 (~3.5 mol% and ~75 mol%, respectively). Relatively oxidizing conditions might promote the reaction of water with the surface of graphite crystals to produce oxygenated functional groups (such as, hydroxyl, epoxy, carboxyl, carbonyl) and hydrogen, which is either adsorbed or released in the fluid as a gas (Blackwood and McGrory, 1958); at most reducing conditions, hydrogen becomes a significant species in the fluid, thus the mechanism of (reversible) dissociative adsorption of hydrogen on graphite active sites, i.e., sites of higher energy such as edges and defects, possibly takes place (Blackwood, 1959; Giberson and Walker, 1966; Barlocco et al., 2020; Vergari and Scarlat, 2021). As a result in both the circumstances graphite surfaces are partly "passivated" and thus the reactivity is decreased. A similar effect was described in the high temperature high pressure (≥750°C, ~50 bar) gasification of pure carbon by reaction with steam and hydrogen: with the increase of hydrogen partial pressure a decrease in the rate of methane production was observed (Blackwood and McGrory, 1958). The kinetic effects described above may be less effective at intermediate fO_2s, such as ΔFMQ ≈ 0 (and probably ΔFMQ ≈ +.2), thus dissolution reactions are

TABLE 3 COH fluid composition obtained from QMS analyses and data used to produce Figure 3 and Figure 4.

Run ID	Starting materials	Buffer	Total volatiles (μmol)	H_2O (μmol)	H_2 (μmol)	CO_2 (μmol)	CO (μmol)	CH_4 (μmol)	$C_{solid\text{-}starting}$ (μmol)	$CM_{dissolved}$ (%)	$[CO_2/(CO_2 + CO + CH_4)]_{molar}$	$[CO/(CO_2 + CO + CH4)]_{molar}$	$[CH_4/(CO_2 + CO + CH_4)]_{molar}$
COH180	graphite + H_2O	HM	31.58	30.05(5)	1.102(9)	0.395(25)	bdl	0.03(3)	363	0.118(7)	0.92(4)	0.00000(23)	0.08(4)
COH145	graphite + H_2O	NNO	4.19	2.4(3)	bdl	0.50(16)	1(3)	0.18(22)	258	0.7(6)	0.27(23)	0.63(31)	0.10(10)
COH189	graphite + H_2O	FMQ	1.69	1.13(24)	bdl	0.27(12)	bdl	0.29(17)	150	0.37(7)	0.49(9)	0.00000(18)	0.51(9)
COH149	graphite + H_2O	WM	0.83	0.693(9)	bdl	0.023(5)	0.12(9)	bdl	345	0.041(13)	0.16(5)	0.84(5)	0.0000(7)
COH181	graphite + H_2O	H_2O-H_2	7.49	1.49(19)	5.65(3)	0.13(9)	bdl	0.22(13)	665	0.052(12)	0.37(11)	0.00000(29)	0.63(11)
COH166	graphite + H_2O	FMQ*	47.72	46.22(6)	0.381(13)	0.98(4)	0.1(6)	bdl	540	0.21(5)	0.88(23)	0.12(23)	0.00000(9)
COH163	GO + H_2O	HM	56.40	45.98(6)	0.358(13)	8.90(4)	1.1(6)	0.08(5)	166	6.1(4)	0.884(26)	0.107(26)	0.0084(23)
COH164	GO + H_2O	NNO	39.83	26.6(3)	bdl	11.99(14)	1(3)	0.06(19)	206	6.4(7)	0.90(9)	0.09(9)	0.005(7)
COH162	GO + H_2O	FMQ	95.35	81.05(3)	bdl	12.529(18)	1.3(3)	0.432(24)	248	5.77(24)	0.876(10)	0.094(10)	0.0302(9)
COH165	GO + H_2O	WM	79.17	67.731(18)	0.550(4)	7.328(11)	1.32(19)	2.233(14)	295	3.69(13)	0.673(6)	0.122(7)	0.2052(18)
COH177	GO + H_2O	H_2O-H2	38.77	24.55(20)	0.56(4)	13.34(10)	bdl	0.23(14)	525	2.60(19)	0.98(7)	0.01(7)	0.017(5)
COH175	MC + H_2O	HM	7.52	6.865(8)	bdl	0.250(4)	0.41(7)	bdl	204	0.322(24)	0.381(21)	0.619(21)	0.00000(15)
COH156	MC + H_2O	NNO	51.08	50.054(14)	bdl	0.682(7)	0.30(13)	0.038(10)	424	0.241(16)	0.67(4)	0.30(4)	0.037(5)
COH154	MC + H_2O	FMQ	0.82	0.776(8)	bdl	0.004(4)	0.04(8)	bdl	352	0.013(11)	0.09(9)	0.91(11)	0.00(6)
COH157	MC + H_2O	WM	0.83	0.778(20)	bdl	0.009(10)	0.04(18)	0.002(14)	548	0.009(17)	0.2(4)	0.8(5)	0.04(16)
COH182	MC + H_2O	H_2O-H_2	10.03	8.929(4)	0.7283(7)	0.1617(21)	bdl	0.209(3)	366	0.1013(28)	0.4363(24)	0.00000(27)	0.5637(24)
COH151	VC + H_2O	HM	25.34	21.364(18)	0.229(4)	3.487(12)	0.26(19)	bdl	312	1.20(5)	0.930(24)	0.070(24)	0.000000(27)
COH152	VC + H_2O	NNO	4.18	3.645(7)	bdl	0.474(3)	0.06(6)	bdl	323	0.164(11)	0.89(5)	0.11(5)	0.00000(19)
COH150	VC + H_2O	FMQ	0.82	0.47(4)	bdl	0.049(19)	0.3(3)	0.01(3)	201	0.17(9)	0.14(7)	0.82(10)	0.04(4)
COH153	VC + H_2O	WM	44.15	42.89(15)	bdl	1.19(8)	bdl	0.07(11)	217	0.58(4)	0.94(4)	0.0000(8)	0.06(4)
COH174	VC + H_2O	H_2O-H_2	4.22	0.88(6)	0.073(10)	0.04(3)	1.0(5)	2.20(4)	318	1.03(9)	0.012(4)	0.31(6)	0.67(5)
COH159	GC + H_2O	HM	19.89	15.05(5)	bdl	4.28(3)	0.5(5)	0.03(4)	688	0.70(4)	0.88(5)	0.11(5)	0.006(4)
COH160	GC + H_2O	NNO	21.76	19.31(5)	bdl	1.87(3)	0.4(5)	0.15(4)	702	0.35(4)	0.76(8)	0.18(9)	0.062(10)
COH158	GC + H_2O	FMQ	18.37	15.60(29)	bdl	2.78(15)	bdl	bdl	1174	0.236(11)	1.00(4)	0.00000(4)	0.00(4)
COH161	GC + H_2O	WM	38.34	35.70(10)	bdl	2.60(5)	bdl	0.04(7)	596	0.443(11)	0.984(13)	0.00000(4)	0.016(13)
COH176	GC + H_2O	H_2O-H_2	24.36	7.59(6)	2.218(10)	0.15(3)	3.2(5)	11.24(4)	521	2.79(7)	0.0103(10)	0.217(14)	0.773(14)

Numbers in parentheses indicate the uncertainty (2σ) in the last digits.
*COH 166 is the only 240 h long run (see Table 2).

10.3389/feart.2023.1013014

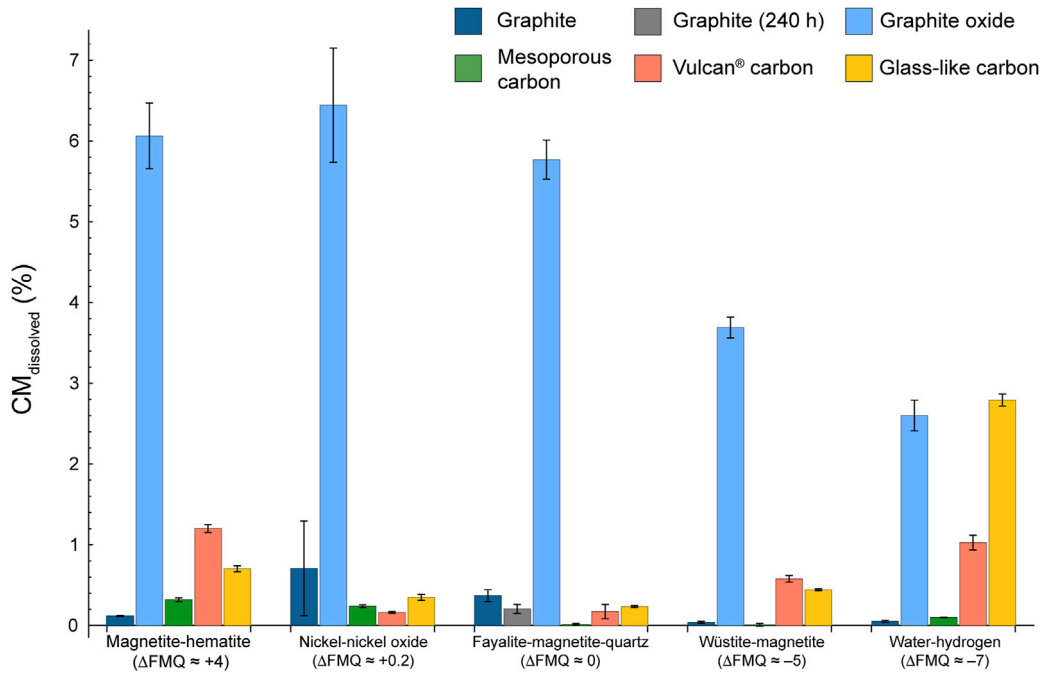

FIGURE 3
$CM_{dissolved}$ in relation to the redox buffer. See the text for the calculation and Table 4 for the data used to produce the figure.

not hindered. A reaction such as such as $2C + 2H_2O = CH_4 + CO_2$ (Cabrera et al., 1982) could describe the similar proportions of CO_2 and CH_4 measured in the fluid ($[CH_4/(CO_2 + CO + CH_4)]_{molar,\ graphite,\ \Delta FMQ \approx 0}$ ~.49, $[CH_4/(CO_2 + CO + CH_4)]_{molar,\ graphite,\ \Delta FMQ \approx 0}$ ~.51). This reaction would be also favored to proceed to the right by the high activity of water that, in equilibrium conditions, would have reached its maximum for fO_2 close to ΔFMQ ≈ 0. Similarly, previous studies reported that the rate of CO_2, CO and CH_4 production is directly proportional to the water partial pressure (Blackwood and McGrory, 1958; Giberson and Walker, 1966). The sluggish reactivity of graphite, already reported in experiments carried out below 700°C (equilibrium with coexisting fluid is not attained even for > 60 days-long runs; Ziegenbein and Johannes, 1980), is confirmed by our results, where the amount of volatile carbon species is comparable in both the 1-h and the 240-h long experiments ($CM_{dissolved}$ = .37 ± .08% vs. .21 ± .06%, respectively) at the same FMQ-buffered conditions. However, we highlight that in the 1 h run at ΔFMQ ≈ 0 (experiment COH189) a supersaturation of carbon volatile species is observed, in that the mole fraction of volatile carbon ($XC_{volatile} = [(CO + CO_2 + CH_4)/(CO + CO_2 + CH_4 + H_2O)]_{molar}$) is ~4 times higher than the equilibrium value ($XC_{volatile\text{-}equilibrium,\ \Delta FMQ \approx 0}$; Supplementary Table S1)). This result can be visualized in Figure 5, where a progress curve of carbon dissolution that fits both the $XC_{volatile}$ in the 240-h long run at ΔFMQ ≈ 0 (experiment COH166) and the $XC_{volatile\text{-}equilibrium,\ \Delta FMQ \approx 0}$ is constructed. The best fit is obtained by setting the rate constant, k, to $.48 \cdot 10^{-6}$ s^{-1} and this value is comparable, though lower, to that obtained for calcium carbonate dissolution experiments at the same P–T conditions ($.8 \cdot 10^{-6}$ s^{-1}; Peng et al., 2022). Supersaturation seems also to occur at ΔFMQ ≈ +.2 (Supplementary Table S1), indicating that in the vicinity of ΔFMQ ≈ 0 a fast dissolution process takes place.

MC, compared to graphite, show a different solubility. At ΔFMQ ≈ −7 MC is ~2 times more soluble than graphite, but similarly produces a mixture of CH_4 and CO_2, where $[CH_4/(CO_2 + CO + CH_4)]_{molar,}$ is ~.6. This probably indicates that MC and graphite undergo similar dissolution reactions, but the elevated intrinsic porosity of MC, which makes available a much greater quantity of active sites, accelerates the reaction rates. At high fO_2s, such as ΔFMQ ≈ +4 and ΔFMQ ≈ +.2, the high availability of active sites may also be responsible for the more elevated CO_2-CO production, in comparison to graphite. In fact, the low concentration of hydrogen in the fluid together with the high H_2-adsorption capacity of MC may drive to the right the reactions (Hunt et al., 1953): $C + H_2O = CO + H_2$; $C + 2H_2O = CO_2 + H_2$; $CO + H_2O = CO_2 + H_2$.

GC and VC show generally higher $CM_{dissolved}$ (>.1% up to ~3%) compared to graphite and MC. As for MC the maxima in the produced volatile carbon species are observed at most oxidizing or reducing conditions, i.e., ΔFMQ ≈ +4 and ΔFMQ ≈ −7. This trend is compatible with thermodynamic models that predict fluids dominantly composed of volatile carbon species at ΔFMQ ≈ +4 and ΔFMQ ≈ −7 (either CO_2 or CH_4, respectively) and close to pure H_2O fluids at ΔFMQ ≈ 0 and ΔFMQ ≈ +.2. The effect of supersaturation at ΔFMQ ≈ 0 is also observed for GC, since $XC_{volatile}$ is ~2 $XC_{volatile\text{-}equilibrium}$ (Supplementary Table S1). Due to the lack of thermodynamic parameters this effect could not be evaluated for VC (as well as for the other CM types). The extensive dissolution of both the carbon forms at ΔFMQ ≈ −7 is associated with high and comparable CH_4 and CO mole fractions ($[CH_4/(CO_2 + CO + CH_4)]_{molar,\ GC,\ \Delta FMQ \approx -7}$ ~ .77, $[CH_4/(CO_2 + CO + CH_4)]_{molar,\ VC,\ \Delta FMQ \approx -7}$ ~ .67, $[CO/(CO_2 + CO + CH_4)]_{molar,\ GC,\ \Delta FMQ \approx -7}$ ~ .22, $[CO/(CO_2 + CO + CH_4)]_{molar,\ VC,\ \Delta FMQ \approx -7}$ ~ .31). As proposed by Blackwood and McGrory (1958), the formation of CO and CH_4 may arise from the combination of the following reactions involving the adsorption of hydrogen and oxygen on carbon surfaces (adsorbed species are enclosed in brackets): $H_2 \rightarrow (H_2)$ (i.e., formation of a hydrogen surface complex); $C + (H_2) + H_2 \rightarrow CH_4$; $C + (H_2) + H_2O \rightarrow (O) + CH_4$; $C + (O) \rightarrow CO$; $C + (O) + H_2O \rightarrow$

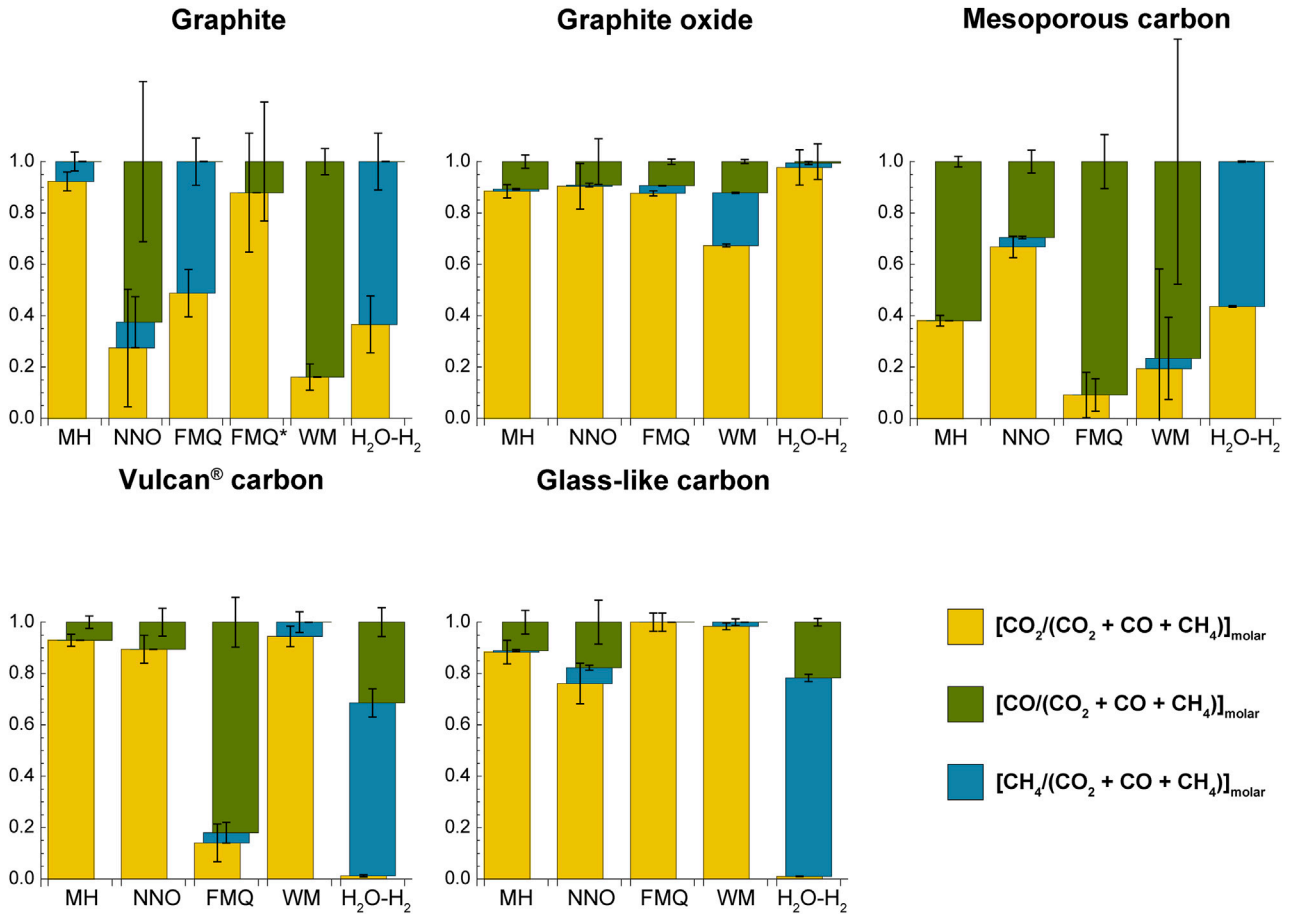

FIGURE 4
Proportion of volatile carbon species in the COH fluid coexisting with the various carbon forms at the specified redox conditions. See the text for the calculation and Table 4 for the data used to produce the figure.

(O) + CO + (H_2); C + (O) + H_2O → (O) + CO + H_2. In the last two reactions, CO is produced from the removal of a preexistent oxygenated functional group, which is then replaced when oxygen from water combines with a neighboring carbon atom having a free orbital; the remaining hydrogen can be released as gas or adsorbed, ultimately participating in methane-forming reactions. The elevated reactivity of GC and VC compared to graphite and MC can be attributed on a first approximation to the abundance of structural defects, deriving from their non-crystalline nature, and to their high content of sp^3-hybridized carbon species (Table 4), which have lower dissociation energies than sp^2 bonded carbon. Moreover, the catalyzing activity of oxygenated functional groups could have a role in increasing the reaction rates, too (e.g., Blackwood, 1959).

Interestingly, at ΔFMQ ≈ −5 all the above carbon forms do not develop pure methane fluids as expected from thermodynamic modelling, but rather the volatile carbon species are dominated by CO_2 for GC and VC ($[CO_2/(CO_2 + CO + CH_4)]_{molar,\ GC,\ \Delta FMQ \approx -5} \sim .98$, $[CO_2/(CO_2 + CO + CH_4)]_{molar,\ VC,\ \Delta FMQ \approx -5} \sim .95$) or CO for graphite and probably MC ($[CO/(CO_2 + CO + CH_4)]_{molar,\ graphite,\ \Delta FMQ \approx -5} \sim .84$, $[CO/(CO_2 + CO + CH_4)]_{molar,\ graphite,\ \Delta FMQ \approx -5} \sim .77$, though this latter number must be considered with caution due to its large uncertainty). Again, the methane-forming reactions seem to be hampered. To account for these effects, we hypothesize that graphite (and presumably for MC) reacts with water to form new hydrogen- and oxygen-containing functional groups that promote CO production (e.g., H_2O → (H_2) + (O) and C + (O) → CO; cf. Blackwood and McGrory, 1958), while GC and VC, which contain a large proportion of oxygenated functional groups, may catalyze reactions that directly produce CO_2 from water or oxidize previously formed CO (e.g., C + H_2O + (O) → (H_2) + CO_2 and (O) + CO → CO_2).

GO is the most reactive carbon form, in that it shows the highest values of $CM_{dissolved}$ (>2%), and produces fluids in which the dominant volatile carbon species is always CO_2. This behavior can be ascribed to its very high proportion of both C(sp^3) (>98 at%) and O heteroatoms (>30 at%; Table 4). It has been shown that by heating GO oxygenated functional groups—i.e., epoxy (C–O–C), carbonyl (C=O), hydroxide (C–OH)—in part decompose and react with carbon to give a gas composed of H_2O, CO, CH_4 and CO_2 (da Silva et al., 2018; He et al., 1998; Zhang et al., 2018) and in part re-organize (hydroxyl and epoxy groups decrease, while carbonyl and cyclic ether groups increase; da Silva et al., 2018). The presence of water also promotes the transformation of the oxygenated groups (Boukhvalov, 2014). At high pressures (≥2.5 GPa) the proportion of the released gas diminishes and GO maintains a high O/C ratio (da Silva et al., 2018). The partial breakdown of functional groups

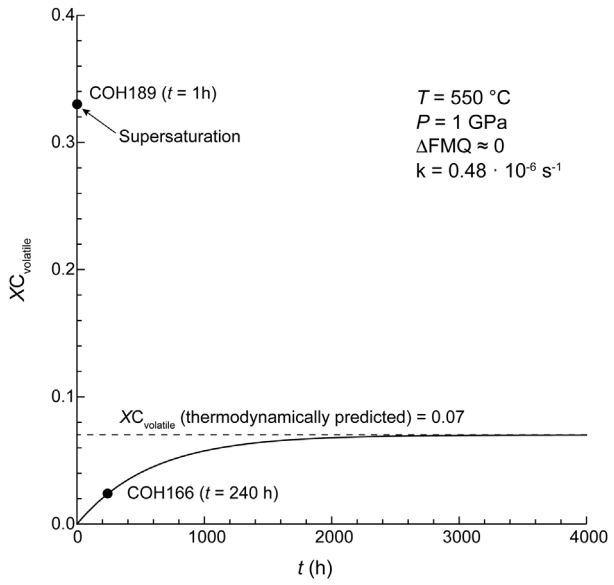

FIGURE 5
Progress curve of graphite dissolution (at 550°C, 1 GPa and ΔFMQ ≈ 0). A rate constant, k, of .48 10^{-6} s^{-1} was chosen to fit both experimental (COH166) and equilibrium (thermodynamically predicted; dashed line) volatile carbon mole fractions in the fluid ($XC_{volatile}$ = (CO + CO_2 + CH_4)/(CO + CO_2 + CH_4 + H_2O)). Equilibrium $XC_{volatile}$ is reached at t > 3,600 h. A supersaturation in dissolved volatile carbon species is observed in the 1 h experimental run (COH189).

accompanied by the reaction of the carbon atoms with volatile carbon species or water leads to the formation of defects (Zhang et al., 2018) that account for the observed decrease of structural order ("amorphization") of GO after our experiments, denoted by the increased intensity of the defect-activated Raman D peak. In addition to this, GO shows a decreasing degree of dissolution from more oxidizing to reducing conditions that is accompanied by a peak of CH_4 at ΔFMQ ≈ −5 ($[CHs_4/(CO_2 + CO + CH_4)]_{molar,\ GO,\ \Delta FMQ \approx -5}$ ~.2). We speculate that these observations may be connected to the presence of relatively high concentrations of free hydrogen in the fluid: hydrogen might replace oxygen in a functional group leading to a C–H bond coupled with a HO* radical that can ultimately react with hydrogen atoms to form water (da Silva et al., 2018), thus preventing carbon extraction to form volatile species; an increase in hydrogen concentration may accelerate this or analogue reactions, that can overcome much sluggish reactions such as those producing CH_4. As a partial confirmation of this, the fluid in contact with GO at ΔFMQ ≈ −7 has the lowest hydrogen concentration ($H_{2\ GO,\ \Delta FMQ \approx -7}$ ~1.5 mol%) among the experiments buffered at the same redox conditions, pointing out to the occurrence of reactions that use up hydrogen.

4.2 Synthetic carbon forms as compositional endmembers of natural CM

The surficial properties of the carbon forms appear to significatively impact the degree of their dissolution and the composition of the fluid they react with. Here, we show that these materials, though synthetic, are valuable as compositional endmembers of natural CM, in terms of sp^2-and sp^3-hybridized carbon proportion and oxygen content. As shown in Figure 6, natural CM (samples DOL and TAV-M938) plots between GO (poorly ordered, C(sp^3)- and O-rich) and graphite (highly ordered, C(sp^2)-rich and O-poor). Kerogen from DOL is closer to GO endmember, having a comparable oxygen concentration (~20 at % and ~31 at%, respectively), a relatively high sp^3-hybridized carbon content (~67 at% vs. 98 at%) and, considering C(sp^3) only, sharing almost the same proportion of functional groups (~43% vs. ~42%). Immature CM, in fact, is rich in oxygen (generally the atomic O/C ratios are comprised between .03 and .3) and in C(sp^3), related to a high proportion of oxygenated functional groups and of aliphatic molecules (Vandenbroucke and Largeau, 2007). Along with the temperature increase that accompanies sediment lithification and metamorphism, CM loses oxygen and develops a more aromatic character, i.e., the proportion of C(sp^2) increases, and organizes into a more ordered structure (e.g., Buseck and Huang, 1985; Vandenbroucke and Largeau, 2007; Buseck and Beyssac, 2014). However, the gain in aromaticity of CM not necessarily leads to a perfectly ordered structure (i.e., graphite), which require further polymerization and structural reorganization (Buseck and Huang, 1985; Buseck and Beyssac, 2014). This is clear in the natural CM sample TAV-M938, which mainly contains C(sp^2) (~81 at%) but it is structurally disordered, being composed of a mixture of diffraction-amorphous microporous and mesoporous textures, the latter being the result of low to moderate grades of metamorphism (Buseck and Huang, 1985; Beyssac et al., 2002b). Both the textures are well approximated by GC and MC (Figures 6, 7A; Table 4). In addition to this, the sample also has a moderate proportion of oxygenated functional groups (~11 at%) similar to that of synthetic GC (~10 at%). VC, instead, would be a more appropriate endmember for disordered C(sp^2)-rich CM that still preserves a higher content of oxygenated functional groups, as is the case for CM produced in COH203 experiment (Figure 7B; Table 4; COH 203 and VC fortuitously share a similar proportion of oxygenated functional groups: ~28 at% and ~30 at%, respectively).

4.3 Geological implications

The observed reaction kinetics of the different carbon forms can have a relevant impact on the dynamics of COH fluid production from the interaction between aqueous fluids and CM in the subduction zones in forearc regions (Figure 8). Tumiati et al. (2020) showed that in the context of a descending slab undergoing dehydration the degree of crystallinity of CM is negatively correlated to the molar proportion of CO_2 released to the fluid up to a depth of ~110 km. Here, we confirm that CM structurally similar to graphite, i.e., composed of crystalline almost pure C(sp^2), generally has a sluggish reactivity in water, while less-ordered C(sp^3)-rich CM reacts faster, particularly towards more oxidizing (ΔFMQ ≈ +4) or reducing (ΔFMQ ≈ −7) conditions. This tendency appears to be emphasized when surface C(sp^3) is bond to oxygen to form functional groups, inasmuch as the fluid in contact with GC, VC or GO has volatile carbon molar concentrations that are up to one order of magnitude higher compared to those in the

TABLE 4 Results of XPS analyses.

	Survey			C 1s			
	C 1s	O 1s	sp^2	sp^3			
				C–C	C–O	C=O	O=C–OH
Graphite							
B.E. (eV)	284.2	531.2	284.4	-	285.8	287.5	-
A.P. (%)	99.4	0.6	99.4	-	0.1	0.5	-
Grapite oxide							
B.E. (eV)	284.1	531.1	284.3	285.2	287.4	290.4	-
A.P. (%)	69.2	30.8	1.7	57.1	34.4	6.8	-
Mesoporous carbon							
B.E. (eV)	284.1	531.1	284.8	-	-	-	-
A.P. (%)	99.6	0.4	93.3	4.6	0.9	0.8	0.4
Vulcan® carbon							
B.E. (eV)	284.5	531.5	284.4	-	285.7	287.1	288.8
A.P. (%)	99	1	70.5	-	17.7	8	3.8
Glass-like carbon							
B.E. (eV)	284.3	532	284.5	285.3	285.9	287.4	288.4
A.P. (%)	92.4	7.6	87.5	2.4	6.3	3	0.8
COH203 (char from microalgae pyrolysis at 1 GPa, 550°C)							
B.E. (eV)	284.6	532.2	284.6	285.3	286.2	287.3	-
A.P. (%)	68.7	15.1	51.1	21	16.9	11	-
DOL (kerogen, ~100°C)							
B.E. (eV)	284.6	532.1	284.5	285.6	286.3	287.9	289.1
A.P. (%)	80.2	19.8	33.2	38.2	18.9	9.1	0.6
TAV-M938 (CM, ~350 °C, 0.6–1 GPa)							
B.E. (eV)	n.d.	n.d.	284.4	285.6	286.7	287.6	288.8
A.P. (%)	n.d.	n.d.	80.5	8.3	7.4	3.1	0.7

B.E., binding energy; A.P., atomic percentage; n.d., not determined

10.3389/feart.2023.1013014

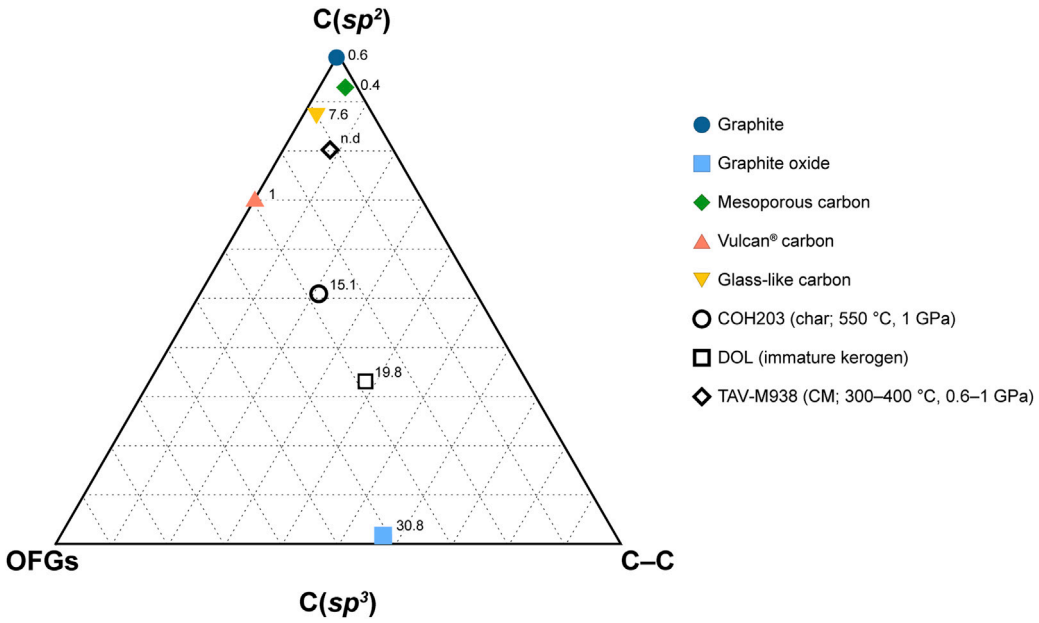

FIGURE 6
Ternary diagram reporting XPS C 1s composition of both synthetic and natural carbonaceous materials. The proportion of sp^3-hybridized carbon is distributed between single C–C bonds and oxygenated functional groups (OFGs). The numbers next to the markers indicate the oxygen content (in at%) as found in XPS survey analysis. The data used for the construction of the figure are listed in Table 4.

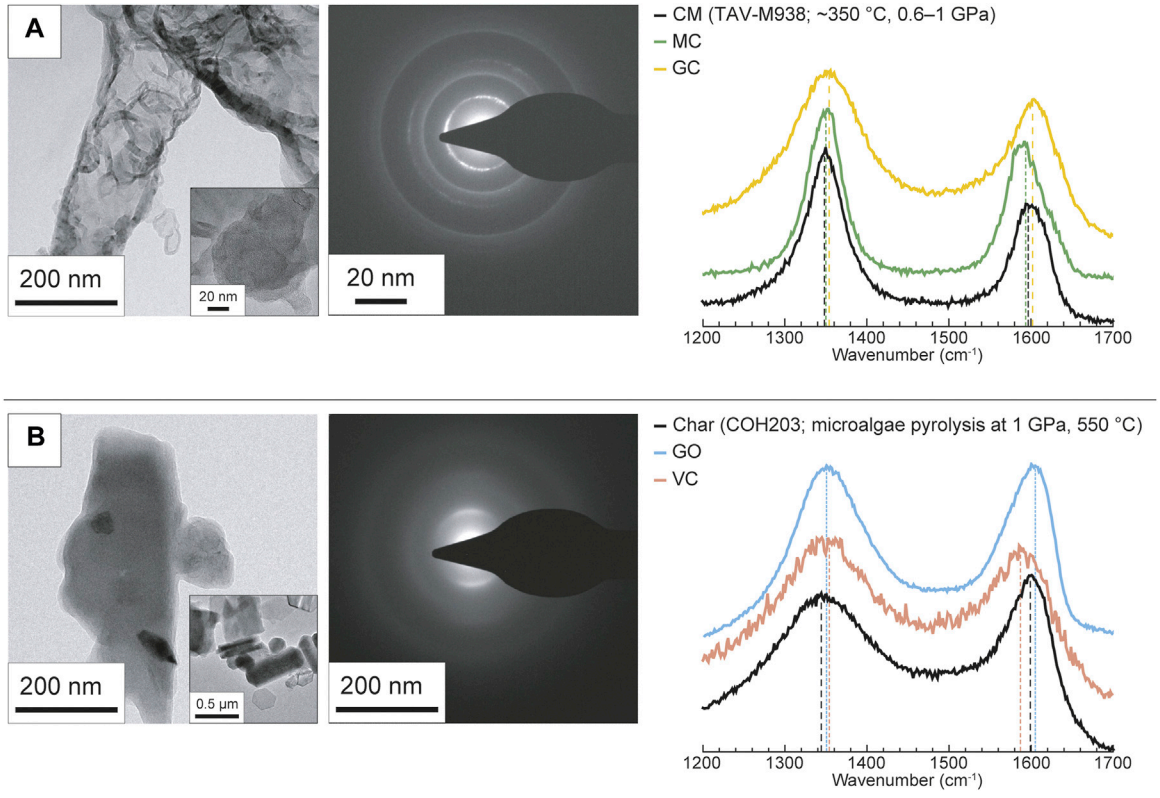

FIGURE 7
Representative TEM images, SAED diffraction patterns and Raman spectra of **(A)** disordered char obtained from pyrolysis of green microalgae at 550°C and 1 GPa (experiment COH203) and **(B)** CM extracted from sample TAV-M938 (300°C–400°C, .6–1 GPa; Vitale Brovarone et al., 2013). The insets show: in **(A)** the local presence of hexagonal graphite crystals; in **(B)** a portion of CM where microporous to "onion-ring like" textures dominate. Raman spectra of GC, GO and MC are reported for comparison.

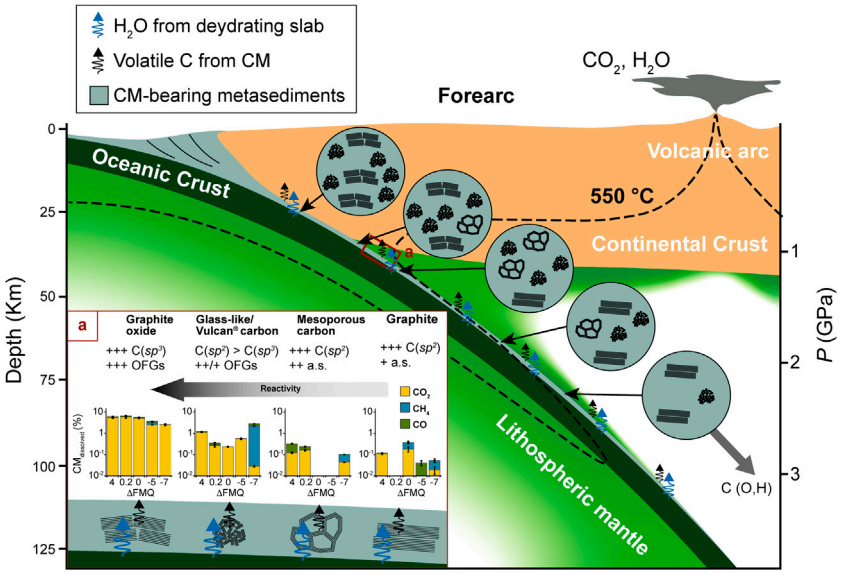

FIGURE 8
Cartoon depicting the fate of CM during subduction. CM rich in sp^3-hybridized carbon and oxygen heteroatoms (such as GO-, GC- and VC-like CM), present as oxygenated functional groups, is likely to react at the shallowest levels and its proportion progressively diminishes with depth. MC-like CM appear as result of low grades of metamorphism and slowly reacts and structurally reorganizes as long as P-T increases. Graphite-like CM forms at high grades and is stable deep in the subduction zone together with some non-graphitizing GC/VC-like CM. A descending flux of solid carbon containing adsorbed O and H may exist. The inset **(A)** summarizes the results of our experimental research by reporting either the most relevant characteristics of the carbon forms and the proportion of $CM_{dissolved}$, for which the contribution of the various volatile carbon species is expressed. Since glass-like and Vulcan® carbon have a similar reactivity, their bar chart is constructed by using a combination of the experimental results, selecting only those showing the highest solubility. Symbols and abbreviations: +++ = high; ++ = moderate; + = low; OFGs = oxygenated functional groups; a.s. = active sites.

experiments containing MC and graphite at the same redox conditions. This has two main effects: 1) aqueous fluids that react with less-ordered CM rich in C(sp^3) and O will contain a higher proportion of dissolved carbon; 2) CM-bearing rocks will experience a removal of less mature CM components if sufficiently high aqueous fluid fluxes are provided. A selective enrichment in graphite-like CM was indeed observed in the blueschist-facies (T ~370°C, P ~1.3 GPa) metasedimentary sequence of Alpine Corsica as a consequence of high time-integrated channelized fluxes along lithological boundaries (Vitale Brovarone et al., 2020). However, our experiments suggest that an opposite scenario could occur at 550°C and 1 GPa, provided that the oxygen content of the CM is relatively low: short CM-water interactions at redox conditions approaching ΔFMQ ≈ 0 enhance the solubility of graphite, which produces 63% more $CM_{dissolved}$ than glass-like carbon. Hence, we hypothesize that at forearc conditions a sufficiently fast rock-water interaction, such as a focused pulse of fluid, may promote preferential dissolution of graphite-like over disordered CM.

Our results show that COH fluid speciation appear to be related to the carbon form water reacts with, redox conditions being equal, because of the peculiar reactions involved. In particular, O- C(sp^3)-rich CM, analogously to GO, would produce CO_2 as main volatile carbon species at redox conditions commonly encountered in subduction zones, meaning that it has the capability to internally buffer the fluid towards relatively oxidizing conditions, as long as oxygen is available for reaction.

Oxygen fugacities set in our experiments are only part of the much wider range of redox conditions recorded in subduction zones: the fO_2 can vary between at least ΔFMQ = −6.0 to +12 at 400°C–550°C and 1–2 GPa in response to local heterogeneities of the rock chemical composition and mineralogy, such as in mélange between the descending slab and the mantle wedge (Tumiati et al., 2015; Vitale Brovarone et al., 2017; Cannaò and Malaspina, 2018; Tumiati and Malaspina, 2019). These values of fO_2 are more prone to be attained in the early stages of dehydration when COH fluids are rock-buffered, i.e., at low fluid-to-rock ratios (Tumiati and Malaspina, 2019). Therefore, we suggest that the solubility of CM that is poorly-organized and rich in sp^3-hybridized carbon, defects and oxygen heteroatoms (i.e., less mature) can be kinetically favored over that of pure crystalline graphite and dominate the organic carbon flux at the onset of dehydration reactions in a forearc environment. Graphite-like CM could indeed be a good candidate as a carbon carrier into the deeper mantle, as other studies reported (e.g., Cook-Kollars et al., 2014), unless the host rocks during their subduction history experienced short interactions with aqueous fluids having an fO_2 approaching that of FMQ buffer. Based on the comparison with the thermodynamic models, we also hypothesize that adsorbed oxygen and hydrogen on carbon surfaces can play a significant role in catalyzing or hampering the reactions that produce carbon volatile species, adding another complexity factor when considering carbon reactivity. Moreover, the high thermal stability of these complexes (da Silva et al., 2018; Vergari and Scarlat, 2021) may also be responsible for a previously neglected flux of O and H atoms associated with CM. To support this, CM from both natural sample TAV-M939 and experiment COH203 preserves a significant proportion of oxygenated functional groups (~11 at% and ~28 at %). Moreover, oxygen- and hydrogen-containing functional groups (e.g., carboxyl and methyl) have been found to coat the surfaces of micro diamonds from Lago di Cignana ultrahigh

pressure metaophiolites (Western Alps; T ~600°C, P > 3 GPa), revealing their stability deep in the subduction zones (Frezzotti et al., 2014; Frezzotti, 2019).

5 Conclusion

The solubility of carbonaceous material at P-T conditions typical of forearc subduction settings arises not only from its crystallinity (with graphite being the only perfectly crystalline carbon form) but also from its surface properties, such as the proportion of sp^2-and sp^3-hybridized carbon, the presence of active sites, the amount of oxygen heteroatoms and the quantity and type of functional groups. The kinetic effects that these factors introduce can lead to significant deviations from thermodynamically predicted composition and speciation of the COH fluids and show a strong dependence on system redox conditions. In particular, our results suggest that:

- The solubility of disordered CM rich in oxygen heteroatoms, C(sp^3) and oxygenated functional groups is generally higher than that of nearly pure C(sp^2) CM (mesoporous or graphite-like carbon); as a consequence, a selective removal of the former is expected when the rock is flushed by a high time-integrated fluid flux (i.e., a channelized flow along lithological boundaries; cf. Vitale Brovarone et al., 2020);
- Dissolution of oxygen-rich (immature) CM may buffer the fluid to rather oxidizing conditions, independently from the initial redox state; thus, in the earliest stages of subduction CO_2 may be the dominant dissolved volatile carbon species;
- Different reactions control the dissolution of the various types of CM at the same redox conditions (e.g., at ΔFMQ ≈ −7 VC/GC and graphite/MC produce a CH_4 + CO and a CH_4 + CO_2 mixture, respectively), affecting the speciation of the COH fluid, and the presence of active sites and/or oxygenated functional groups has a key role in their catalyzation; in particular, passivation of active sites may be related to graphite sluggish reactivity, and this process seems to be less effective for short-lived carbon-water interaction (i.e., fluid injection);
- Some of the oxygen(and hydrogen)-containing functional groups both inherited from precursor organic matter and produced by carbon-water reactions can be stable at the investigated conditions; thus, a flux of oxygen (and H) may be associated with CM subduction.

Data availability statement

The original contributions presented in the study are included in the article/Supplementary Material, further inquiries can be directed to the corresponding author.

Author contributions

LT interpreted the experimental results and wrote the manuscript. ST conceived the experimental study and critically participated to the data interpretation. ST, AA, and FM collected the QMS data. AV carried out and interpreted the XPS analyses and provided suitable starting materials to be utilized in the experimental runs. PF helped in the acquisition and interpretation of the Raman spectra of carbonaceous materials. AA and FM prepared and handled the experiments.

Acknowledgments

We thank Nicola Rotiroti (Dipartimento di Scienze della Terra "Ardito Desio", University of Milan, Milan, Italy) for the TEM analysis of carbonaceous materials. We are also grateful to Alberto Vitale Brovarone (Dipartimento di Scienze Biologiche, Geologiche e Ambientali, University of Bologna, Bologna, Italy) for providing sample TAV-M938. ST acknowledges support from the Italian program MIUR PRIN 2017ZE49E7_002. LT acknowledges the APC fund of the University of Milan.

Conflict of interest

The authors declare that the research was conducted in the absence of any commercial or financial relationships that could be construed as a potential conflict of interest.

Publisher's note

Supplementary material

The Supplementary Material for this article can be found online at: https://www.frontiersin.org/articles/10.3389/feart.2023.1013014/full#supplementary-material

SUPPLEMENTARY FIGURE S1
Oxygen fugacity imposed by the different buffers calculated between 550 and 551°C at 1 GPa.

SUPPLEMENTARY FIGURE S2
Representative TEM images and SAED diffraction patterns of starting **(A)** graphite and **(B)** glass-like carbon and comparison between their Raman spectra before and after the experiments. The intensities of the Raman spectra are normalized to the same scale.

SUPPLEMENTARY FIGURE S3
Mole fractions of volatile carbon species in the COH fluid coexisting with the various carbon forms at the specified redox conditions. In contrast to Figure 4, here the sum of fluid species in the denominator includes H_2O ($X_{species}$ = $n_{species}/(n_{H2O} + n_{CO} + n_{CO2} + n_{CH4})$, where $n_{species}$ is the number of moles of one among CO, CO_2, CH_4).

SUPPLEMENTARY FIGURE S4
Raman spectrum of kerogen from DOL sample.

References

Barlocco, I., Capelli, S., Lu, X., Tumiati, S., Dimitratos, N., Roldan, A., et al. (2020). Role of defects in carbon materials during metal-free formic acid dehydrogenation. *Nanoscale* 12, 22768–22777. doi:10.1039/d0nr05774f

Berra, F., Azmy, K., and Della Porta, G. (2020). Stable-isotope and fluid inclusion constraints on the timing of diagenetic events in the dolomitized Dolomia Principale inner platform (Norian, Southern Alps of Italy). *Mar. Petroleum Geol.* 121, 104615. doi:10.1016/j.marpetgeo.2020.104615

Berra, F., and Carminati, E. (2010). Subsidence history from a backstripping analysis of the permo-mesozoic succession of the central southern Alps (northern Italy). *Basin Res.* 22, 952–975. doi:10.1111/j.1365-2117.2009.00453.x

Beyssac, O., Goffé, B., Chopin, C., and Rouzaud, J. N. (2002a). Raman spectra of carbonaceous material in metasediments: A new geothermometer. *J. Metamorph. Geol.* 20, 859–871. doi:10.1046/j.1525-1314.2002.00408.x

Beyssac, O., Rouzaud, J. N., Goffe, B., Brunet, F., and Chopin, C. (2002b). Graphitization in a high-pressure, low-temperature metamorphic gradient: A Raman microspectroscopy and HRTEM study. *Contributions Mineralogy Petrology* 143, 19–31. doi:10.1007/s00410-001-0324-7

Beyssac, O., Goffé, B., Petitet, J. P., Froigneux, E., Moreau, M., and Rouzaud, J. N. (2003). On the characterization of disordered and heterogeneous carbonaceous materials by Raman spectroscopy. *Spectrochimica Acta Part A Mol. Biomol. Spectrosc.* 59, 2267–2276. doi:10.1016/s1386-1425(03)00070-2

Beyssac, O., and Lazzeri, M. (2012). Application of Raman spectroscopy to the study of graphitic carbons in the Earth sciences. *Eur. Mineralogical Union Notes Mineralogy* 12, 415–454.

Beyssac, O., and Rumble, D. (2014). Graphitic carbon: A ubiquitous, diverse, and useful geomaterial. *Elements* 10, 415–420. doi:10.2113/gselements.10.6.415

Blackwood, J. D., and McGrory, F. (1958). The carbon-steam reaction at high pressure. *Aust. J. Chem.* 11, 16–33. doi:10.1071/ch9580016

Blackwood, J. D. (1959). The reaction of carbon with hydrogen at high pressure. *Aust. J. Chem.* 12, 14–28. doi:10.1071/ch9590014

Bose, K., and Ganguly, J. (1995). Quartz-coesite transition revisited: Reversed experimental determination at 500–1200 °C and retrieved thermochemical properties. *Am. Mineralogist* 80 (3-4), 231–238. doi:10.2138/am-1995-3-404

Boukhvalov, D. W. (2014). Oxidation of a graphite surface: The role of water. *J. Phys. Chem. C* 118, 27594–27598. doi:10.1021/jp509659p

Brovarone, A. V., Beyssac, O., Malavieille, J., Molli, G., Beltrando, M., and Compagnoni, R. (2013). Stacking and metamorphism of continuous segments of subducted lithosphere in a high-pressure wedge: The example of alpine Corsica (France). *Earth-Science Rev.* 116, 35–56. doi:10.1016/j.earscirev.2012.10.003

Buseck, P. R., and Beyssac, O. (2014). From organic matter to graphite: Graphitization. *Elements* 10, 421–426. doi:10.2113/gselements.10.6.421

Buseck, P. R., and Huang, B. J. (1985). Conversion of carbonaceous material to graphite during metamorphism. *Geochimica Cosmochimica Acta* 49, 2003–2016. doi:10.1016/0016-7037(85)90059-6

Cabrera, A. L., Heinemann, H., and Somorjai, G. A. (1982). Methane production from the catalyzed reaction of graphite and water vapor at low temperatures (500–600 K). *J. Catal.* 75, 7–22. doi:10.1016/0021-9517(82)90117-8

Cannaò, E., and Malaspina, N. (2018). From oceanic to continental subduction: Implications for the geochemical and redox evolution of the supra-subduction mantle. *Geosphere* 14, 2311–2336. doi:10.1130/ges01597.1

Cook-Kollars, J., Bebout, G. E., Collins, N. C., Angiboust, S., and Agard, P. (2014). Subduction zone metamorphic pathway for deep carbon cycling: I. Evidence from HP/UHP metasedimentary rocks, Italian. *Alps. Chemical Geology* 386, 31–48.

Connolly, J. A. D., and Cesare, B. (1993). C-O-H-S fluid composition and oxygen fugacity in graphitic metapelites. *J. Metamorph. Geol.* 11, 379–388. doi:10.1111/j.1525-1314.1993.tb00155.x

Connolly, J. A. D. (1995). Phase diagram methods for graphitic rocks and application to the system C-O-H-FeO-TiO_2-SiO_2. *Contributions Mineralogy Petrology* 119, 94–116. doi:10.1007/bf00310720

Connolly, J. A. D. (2005). Computation of phase equilibria by linear programming: A tool for geodynamic modeling and its application to subduction zone decarbonation. *Earth Planet. Sci. Lett.* 236, 524–541. doi:10.1016/j.epsl.2005.04.033

da Silva, A. F., Christmann, A. M., Costa, T. M. H., Muniz, A. R., and Balzaretti, N. M. (2018). Thermal annealing of graphite oxide under high pressure: An experimental and computational study. *Carbon* 139, 1035–1047. doi:10.1016/j.carbon.2018.08.006

Eugster, H. P. (1957). Heterogeneous reactions involving oxidation and reduction at high pressures and temperatures. *J. Chem. Phys.* 26, 1760–1761. doi:10.1063/1.1743626

Eugster, H. P., and Skippen, G. B. (1967). Igneous and metamorphic reactions involving gas equilibria. *Res. Geochem.* 2, 492–520.

Frezzotti, M. L. (2019). Diamond growth from organic compounds in hydrous fluids deep within the Earth. *Nat. Commun.* 10, 4952–4958. doi:10.1038/s41467-019-12984-y

Frezzotti, M. L., Huizenga, J. M., Compagnoni, R., and Selverstone, J. (2014). Diamond formation by carbon saturation in C–O–H fluids during cold subduction of oceanic lithosphere. *Geochimica Cosmochimica Acta* 143, 68–86. doi:10.1016/j.gca.2013.12.022

Frost, B. R. (1991). "Introduction to oxygen fugacity and its petrologic importance," in *Oxide mineral*. Editor D. H. Lindsley (Berlin: De Gruyter), 1–10.

Giberson, R. C., and Walker, J. P. (1966). Reaction of nuclear graphite with water vapor part I. Effect of hydrogen and water vapor partial pressures. *Carbon* 3, 521–525. doi:10.1016/0008-6223(66)90037-6

Hayes, J. M., and Waldbauer, J. R. (2006). The carbon cycle and associated redox processes through time. *Philosophical Trans. R. Soc. B Biol. Sci.* 361, 931–950. doi:10.1098/rstb.2006.1840

Hazen, R. M., Downs, R. T., Jones, A. P., and Kah, L. (2013). Carbon mineralogy and crystal chemistry. *Rev. Mineralogy Geochem.* 75, 7–46. doi:10.2138/rmg.2013.75.2

He, H., Klinowski, J., Forster, M., and Lerf, A. (1998). A new structural model for graphite oxide. *Chem. Phys. Lett.* 287, 53–56. doi:10.1016/s0009-2614(98)00144-4

Holland, T. J. B., and Powell, R. (1998). An internally consistent thermodynamic data set for phases of petrological interest. *J. Metamorph. Geol.* 16, 309–343. doi:10.1111/j.1525-1314.1998.00140.x

Holleck, G. L. (1970). Diffusion and solubility of hydrogen in palladium and palladium-silver alloys. *J. Phys. Chem.* 74, 503–511. doi:10.1021/j100698a005

Hunt, B. E., Mori, S., Katz, S., and Peck, R. E. (1953). Reaction of carbon with steam at elevated temperatures. *Industrial Eng. Chem.* 45, 677–680. doi:10.1021/ie50519a054

Luque, F. J., Pasteris, J. D., Wopenka, B., Rodas, M., and Barrenechea, J. F. (1998). Natural fluid-deposited graphite: Mineralogical characteristics and mechanisms of formation. *American Journal of Science* 298, 471–498.

Mason, E., Edmonds, M., and Turchyn, A. V. (2017). Remobilization of crustal carbon may dominate volcanic arc emissions. *Science* 357, 290–294. doi:10.1126/science.aan5049

Miozzi, F., and Tumiati, S. (2020). Aqueous concentration of CO_2 in carbon-saturated fluids as a highly sensitive oxybarometer. *Geochem. Perspect. Lett.* 16, 30–34. doi:10.7185/geochemlet.2040

Myers, J., and Eugster, H. P. (1983). The system Fe-Si-O: Oxygen buffer calibrations to 1, 500K. *Contributions Mineralogy Petrology* 82, 75–90. doi:10.1007/bf00371177

Nylén, J., Sato, T., Soignard, E., Yarger, J. L., Stoyanov, E., and Häussermann, U. (2009). Thermal decomposition of ammonia borane at high pressures. *J. Chem. Phys.* 131, 104506. doi:10.1063/1.3230973

Peng, W., Tumiati, S., Zhang, L., Tiraboschi, C., Vitale Brovarone, A., Toffolo, L., et al. (2022). An experimental study on kinetics-controlled Ca-carbonate aqueous reduction into CH_4 (1 and 2 GPa, 550° C): Implications for C mobility in subduction zones. *J. Petrology* 63, 1–18. doi:10.1093/petrology/egac070

Plank, T., and Manning, C. E. (2019). Subducting carbon. *Nature* 574, 343–352. doi:10.1038/s41586-019-1643-z

Shaw, H. R. (1963). Hydrogen-water vapor mixtures: Control of hydrothermal atmospheres by hydrogen osmosis. *Science* 139, 1220–1222. doi:10.1126/science.139.3560.1220

Sheik, C. S., Cleaves, H. J., Johnson-Finn, K., Giovannelli, D., Kieft, T. L., Papineau, D., et al. (2020). Abiotic and biotic processes that drive carboxylation and decarboxylation reactions. *Am. Mineralogist* 105, 609–615. doi:10.2138/am-2020-7166ccbyncnd

Shiell, T. B., McCulloch, D. G., McKenzie, D. R., Field, M. R., Haberl, B., Boehler, R., et al. (2018). Graphitization of glassy carbon after compression at room temperature. *Phys. Rev. Lett.* 120, 215701. doi:10.1103/physrevlett.120.215701

Sonwane, C. G., Wilcox, J., and Ma, Y. H. (2006). Achieving optimum hydrogen permeability in PdAg and PdAu alloys. *J. Chem. Phys.* 125, 184714. doi:10.1063/1.2387166

Sverjensky, D. A., Stagno, V., and Huang, F. (2014). Important role for organic carbon in subduction-zone fluids in the deep carbon cycle. *Nat. Geosci.* 7, 909–913. doi:10.1038/ngeo2291

Thommes, M., Kaneko, K., Neimark, A. V., Olivier, J. P., Rodriguez-Reinoso, F., Rouquerol, J., et al. (2015). Physisorption of gases, with special reference to the evaluation of surface area and pore size distribution (IUPAC Technical Report). *Pure Appl. Chem.* 87, 1051–1069. doi:10.1515/pac-2014-1117

Tiraboschi, C., Miozzi, F., and Tumiati, S. (2022). Carbon-saturated COH fluids in the upper mantle: a review of high-pressure and high-temperature ex situ experiments. *Eur. J. Mineral.* 34, 59–75. doi:10.5194/ejm-34-59-2022

Tiraboschi, C., Tumiati, S., Recchia, S., Miozzi, F., and Poli, S. (2016). Quantitative analysis of COH fluids synthesized at HP–ht conditions: An optimized methodology to measure volatiles in experimental capsules. *Geofluids* 16, 841–855. doi:10.1111/gfl.12191

Tuinstra, F., and Koenig, J. L. (1970). Raman spectrum of graphite. *J. Chem. Phys.* 53, 1126–1130. doi:10.1063/1.1674108

Tumiati, S., Godard, G., Martin, S., Malaspina, N., and Poli, S. (2015). Ultra-oxidized rocks in subduction mélanges? Decoupling between oxygen fugacity and oxygen availability in a Mn-rich metasomatic environment. *Lithos* 226, 116–130. doi:10.1016/j.lithos.2014.12.008

Tumiati, S., Tiraboschi, C., Sverjensky, D. A., Pettke, T., Recchia, S., Ulmer, P., et al. (2017). Silicate dissolution boosts the CO_2 concentrations in subduction fluids. *Nat. Commun.* 8, 1–11. doi:10.1038/s41467-017-00562-z

Tumiati, S., Zanchetta, S., Pellegrino, L., Ferrario, C., Casartelli, S., and Malaspina, N. (2018). Granulite-facies overprint in garnet peridotites and kyanite eclogites of monte duria (central Alps, Italy): Clues from srilankite-and sapphirine-bearing symplectites. *J. Petrology* 59, 115–151. doi:10.1093/petrology/egy021

Tumiati, S., Tiraboschi, C., Miozzi, F., Vitale Brovarone, A., Manning, C. E., Sverjensky, D. A., et al. (2020). Dissolution susceptibility of glass-like carbon versus crystalline graphite in high-pressure aqueous fluids and implications for the behavior of organic matter in subduction zones. *Geochimica Cosmochimica Acta* 273, 383–402. doi:10.1016/j.gca.2020.01.030

Tumiati, S., Recchia, S., Remusat, L., Tiraboschi, C., Sverjensky, D. A., Manning, C. E., et al. (2022). Subducted organic matter buffered by marine carbonate rules the carbon isotopic signature of arc emissions. *Nat. Commun.* 13, 2909–2910. doi:10.1038/s41467-022-30421-5

Tumiati, S., and Malaspina, N. (2019). Redox processes and the role of carbon-bearing volatiles from the slab–mantle interface to the mantle wedge. *J. Geol. Soc.* 176, 388–397. doi:10.1144/jgs2018-046

Vandenbroucke, M., and Largeau, C. (2007). Kerogen origin, evolution and structure. *Org. Geochem.* 38, 719–833. doi:10.1016/j.orggeochem.2007.01.001

Vergari, L., and Scarlat, R. O. (2021). Thermodynamics of hydrogen in graphite at high temperature and the effects of oxidation, irradiation and isotopics. *J. Nucl. Mater.* 552, 152797. doi:10.1016/j.jnucmat.2021.152797

Vitale Brovarone, A., Martinez, I., Elmaleh, A., Compagnoni, R., Chaduteau, C., Ferraris, C., et al. (2017). Massive production of abiotic methane during subduction evidenced in metamorphosed ophicarbonates from the Italian Alps. *Nat. Commun.* 8, 1–13. doi:10.1038/ncomms14134

Vitale Brovarone, A., Tumiati, S., Piccoli, F., Ague, J. J., Connolly, J. A., and Beyssac, O. (2020). Fluid-mediated selective dissolution of subducting carbonaceous material: Implications for carbon recycling and fluid fluxes at forearc depths. *Chem. Geol.* 549, 119682. doi:10.1016/j.chemgeo.2020.119682

Xie, F. Y., Xie, W. G., Gong, L., Zhang, W. H., Chen, S. H., Zhang, Q. Z., et al. (2010). Surface characterization on graphitization of nanodiamond powder annealed in nitrogen ambient. *Surf. Interface Analysis* 42, 1514–1518. doi:10.1002/sia.3350

Zhang, C., and Duan, Z. (2010). GFluid: An Excel spreadsheet fori nvestigating C-O-H fluid composition under high temperatures and pressures. *Comput. Geosciences* 36, 569–572. doi:10.1016/j.cageo.2009.05.008

Zhang, G., Wen, M., Wang, S., Chen, J., and Wang, J. (2018). Insights into thermal reduction of the oxidized graphite from the electro-oxidation processing of nuclear graphite matrix. *RSC Adv.* 8, 567–579. doi:10.1039/c7ra11578d

Ziegenbein, D., and Johannes, W. (1980). Graphite in C-H-O fluids: An unsuitable compound to buffer fluid composition at temperatures up to 700 °C. *Neues Jahrb. für Mineral. Monatsh.* 7, 289–305.

Appendix A Main features of synthetic and natural CM

The five synthetic carbon forms are characterized by distinct microtextures, crystallinity, carbon hybridization, content of oxygen heteroatoms and type of oxygenated functional groups, as described below (cf. Table 4).

Graphite (Supplementary Figure S2A) forms aggregates of ~5 nm-thick sub-circular platelets that have diameter of few to several tens of nanometers and in cross section have a layered structure. It is perfectly crystalline, as shown by the presence of hkl reflections in the SAED pattern. The Raman spectrum is dominated by a sharp and intense G peak at ~1,574 cm^{-1}; D peak at 1,345 cm^{-1} is broad and weak. Graphite is almost pure sp^2-hybridized carbon (O < 1 at%).

Graphite oxide (GO) (Figure 2A) is composed of sheets with a thickness up to a few tenths of nanometers that locally show a layered organization, i.e., the presence of some large (up to ~10 nm) crystalline domains. This partial ordering is indicated by the presence of modulations of the diffraction bands in the SAED pattern (Beyssac et al., 2002b). Its Raman spectrum shows two similarly intense D and G peaks, at ~1,354 cm^{-1} and ~1,605 cm^{-1}, respectively. GO has the highest concentration of sp^3-hybridized carbon (~98 at%) and oxygen heteroatoms (~31 at%). In GO a large proportion of C(sp^3) is related to the presence oxygenated functional groups (~41 at%).

Mesoporous carbon (MC) (Figure 2B) is made of ~5 nm thick carbon layers wrapped into polygonal shapes, which enclose pores with a diameter comprised between few nanometers and 15–20 nm. The SAED patterns show sharp and intense diffraction bands. Its Raman spectrum is characterized by D and G positioned at ~1,340 cm^{-1} and ~1,576 cm^{-1}, respectively, with the former being more intense than the latter. MC is nearly pure carbon (O < 1 at %), composed of dominant sp^2-hybridized carbon (~93 at%) and a small proportion of C(sp^3) mainly related to C–C bonds (~5 at%).

Vulcan® carbon (VC) (Figure 2C) is composed of rounded particles with a diameter of ~50 nm and a vague concentric layered structure. The low degree of structural organization is denoted by the presence of wide and weak diffraction bands in SAED patterns. Its Raman spectrum shows broad and similarly intense D and G peaks at ~1,356 cm^{-1} and~1,588 cm^{-1}, respectively. VC has a high proportion of sp^3-hybridized carbon (~29 at%), which is entirely due to the presence of oxygenated functional groups.

Glass-like carbon (GC) (Supplementary Figure S2B) consists of a nanometer-scale tangle of graphitic sheets (cf. Shiell et al., 2018). As a consequence of this low degree of atomic organization, the related SAED pattern shows very faint and broad diffraction bands, indistinguishable from that of the holey amorphous carbon support grid. In the Raman spectrum D and G peaks, positioned at ~1,354 cm^{-1} and ~1,602 cm^{-1}, respectively, are both broad, but the former is more intense than the latter. GC contains a small proportion of oxygen heteroatoms (~8 at%) and it is principally composed of sp^2-hybridized carbon (~88 at%). The remaining C(sp^3) mainly forms oxygenated functional groups.

Char was produced from the pyrolysis at 550°C and 1 GPa of green microalgae (experiment COH203). Char is disordered—the Raman spectrum shows a broad D peak at ~1,344 cm^{-1} and a more intense and narrower G peak at ~1,600 cm^{-1} –, but locally some small hexagonal graphite crystals (diameter ≤ 300 μm) can be found (Figure 7B). The char surface has a moderate proportion of oxygen heteroatoms (~18 at%) and an approximately equal content of sp^2-and sp^3-hybridized carbon species (~51 at% and ~49 at%, respectively), whose greatest part (~30 at%) is related to the presence of oxygenated functional groups.

Kerogen extracted from natural sample DOL has a Raman spectrum characterized by high background fluorescence from which a broad D peak at ~1,350 cm^{-1} and a quite sharp G peak at ~1,579 cm^{-1} emerge (Supplementary Figure S4). Kerogen has a high content of oxygen heteroatoms (~20 at%) and large proportion of sp^3-hybridized carbon (~67 at%), part of which occurs as oxygenated functional groups (~29 at%).

CM separated from natural sample TAV-M938 (Figure 7A) is structurally and texturally heterogeneous at a <1 μm scale: it is mainly disordered material, characterized by both concentric layered and mesoporous textures, but locally exhibits ordered graphite-like portions. The Raman spectrum shows a broad and intense D peak at ~1,350 cm^{-1} and narrower and less intense G peak at 1,604 cm^{-1}. CM has a high proportion of sp^2-hybridized carbon (~81 at%); the remainder C(sp^3) forms both C–C bonds (~8 at%) and oxygenated functional groups (~11 at%). The total content of oxygen heteroatoms could not be evaluated because of the interference with oxygen from associated silicates.